https://dx.doi.org/10.1016/j.surfin.2022.101903

Review on thin film coatings for precision glass molding

Awais AKHTAR, Haihui RUAN*

Department of Mechanical Engineering, The Hong Kong Polytechnic University, Hung Hom, Kowloon, Hong Kong, China

Abstract

Precision glass molding (PGM) is an advanced glass manufacturing technology employed by the optical industry for the large-scale production of lenses and other precision glass components. One of the key breakthroughs is the use of anti-sticking coatings that extend the tool life and render a molded glass surface polish-free. In the literature, various protective coatings, including noble metals, ceramics, and diamond-like carbon (DLC) coatings, have been attempted. These coatings met with varying degree of success and have finite service life due to various degradation mechanisms. Noble metal coatings, although expensive, are the most preferred owing to their simplicity of fabrication and high operating temperatures. Their degradation starts from the diffusion and segregation of active elements along grain boundaries. Most of attempted ceramic coatings are deteriorated because the oxidation of metallic elements—that occurs more easily than noble metals—develops an oxide scale that is adhesive to glass. DLC coatings exhibits poor thermal stability at high temperatures (> 600 °C) owing to the strong tendency of graphitization and inadequacy in developing high sp^3-content; their application in PGM is limited. The improvement in oxidation resistance and anti-sticking of coatings is a continuous development task, particularly when the PGM technology is to be adapted for glasses with high glass transition temperature. This paper reviews the state of the art of these coatings with a focus on their deposition techniques, anti-sticking, microstructural and mechanical properties, and their degradation mechanisms in glass molding cycles. With these explorations, a perspective on further improving the reliability of PGM coatings is provided.

Keywords: coatings, sputtering, anti-sticking property, substrate, mechanical property

* Corresponding author Tel.: + 852 2766 6648, Fax: +852 2365 4703, E-mail address: haihui.ruan@polyu.edu.hk

1. Introduction

With the increasing applications of optical components in various fields, such as consumer electronics, lasers, and medical technology, the precision glass manufacturing that achieves superior surface quality and optical effectiveness is in large demand in the industry [1-3]. Compared with traditional grinding and polishing methods, precision glass molding (PGM) is currently the most appropriate and widely recognized technology for the cost-effective mass production of precision glass components such as lenses and optical switches [4-6]. In a PGM process, high-precision mold inserts directly contact heated glass above its glass transition temperature (T_g) under mechanical loading. The occurrence of physical diffusion and chemical reactions on the glass–mold contact area at molding temperatures results in premature mold failure and significantly affects the surface quality of the glass [7]. Thus, the application of protective coating is critical for extending the service lifespan of the molds and increasing the surface quality of molded glass lenses [8]. The synthesis of protective surface coatings has gained increasing popularity owing to their exceptional physicochemical properties required in optical, magnetic, and electrical applications [9-12]. Among them, an important coating development is to enable molded precision optics that shift the optical industry from the conventional expensive and time-consuming manufacturing processes via grinding, polishing, and lapping [13, 14] to an efficient and scalable PGM technology. Surface protective coatings for PGM are critical for advancing PGM into a single-step process in mass production [15], which must withstand thermomechanical stresses and a corrosive thermochemical environment owing to the softened glass at molding temperatures [8]. Therefore, the structural behaviors of these coatings should exhibit sufficient strength and hardness to resist thermal shocks, adhesion, and wear at high temperatures [16].

For PGM, three major groups of surface protective coatings are used: (*i*) noble metal coatings [17], (*ii*) ceramic hard coatings [18], and (*iii*) carbon-based (e.g., diamond-like carbon (DLC)) coatings [19]. Several studies on various anti-adhesion surface coatings have been conducted with varying degrees of success for particular glass types. However, glass-sticking, thermal instability, and oxidation of the coating elements at molding temperatures—at which the viscosity of glass reduces to 10^7 - 10^9 Pa.s—remain major challenges.

Although several coatings for PGM have been used, their failure mechanisms have been fragmentedly discussed in the literature. As the current trend of PGM migrates towards glass with high glass transition points, such as the aluminosilicate glass used in portable electronics, there is a need to consolidate the existing know-how and, if possible, to improve the high-

temperature performance for more stringent applications. Therefore, this paper reviews studies on coatings for PGM. We describe the deposition techniques, microstructural evolutions, and their mechanical performances, and then present our perspective on the optimization of coating durability, cost-effectiveness, and high-temperature performance.

2. Deposition techniques

Thin films exhibit distinctive performances compared with bulk materials because the majority of the deposition processes are nonequilibrium in nature; thus, a thin film formation can be outside the permissible region of the corresponding (equilibrium) phase diagram [20-22]. Deposition techniques practically determine the properties of a thin film and can be used to modify the properties of the bulk material. These techniques require proper consideration according to the area of utilization because they do not result in identical properties, such as surface morphology, microstructure, hardness, and corrosion resistance [23]. Thin film deposition is broadly categorized into two main groups: physical vapor deposition (PVD) and chemical vapor deposition (CVD) (Fig. 1). For PGM, the coatings developed based on them in the open literature have been summarized in Table 1.

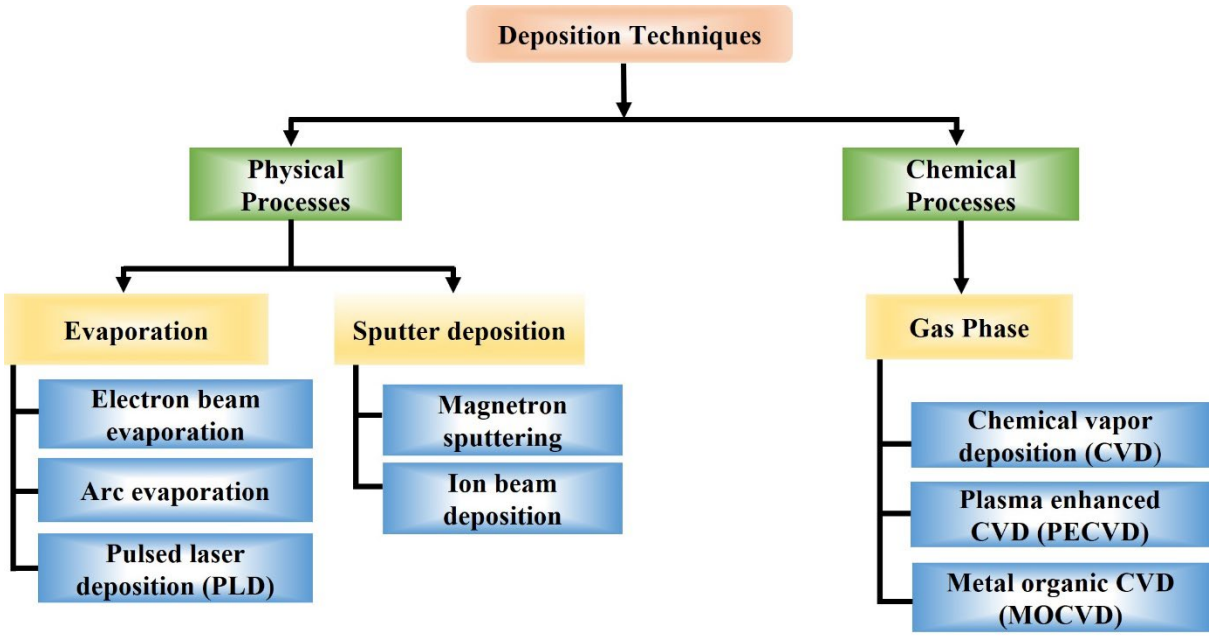

Figure 1. Classification of deposition techniques

2.1 Physical vapor deposition

PVD encompasses a broad range of vapor-phase technologies, where atoms or molecules are physically ejected from a material and subsequently condensed and nucleated onto a substrate [24]. Generally, PVD methods are employed in film deposition with thicknesses

ranging from several nanometers to several micrometers. Their applications include graded composition deposits, multilayer coatings, free-standing structures, and dense deposits. Owing to their versatile features, sustainable and environment-friendly PVD methods have received increasing interest in modern times [25]. It is employed primarily to improve the tribological, optical, and mechanical properties of a substrate material [26, 27]. The main PVD processes are sputtering, electron beam evaporation, and ion beam deposition.

2.1.1 Sputtering

Sputtering is a vacuum coating technique in which cathodic targets (source materials) are bombarded by energetic ions of inert gases such as argon or helium. The development of cations is caused by the plasma that ignites between the targets (cathode) and substrates (anode). The positive ions (cations) being accelerated in an electric field strike the surface of a target [28]; the transfer of kinetic energy to the target atoms establishes a thin film onto a substrate surface (Fig. 2). This process has several advantages, such as high purity, remarkable adhesion, high deposition rates, and simplicity of depositing either metallic or ceramic coatings. Sputtering also facilitates the formation of materials with a high melting point. Reactive gases, such as oxygen or nitrogen, can be added to form metal oxides, nitrides, or other compound films. Generally, the sputtering process has common types: direct current (DC) and radio frequency (RF) sputtering. In a DC sputtering system, the glow discharge is maintained by a DC current between the metallic electrodes. However, in RF sputtering, an AC current is applied to neutralize the charge build-up in an insulating target material.

Table 1 lists the PGM coatings reported in the literature. We can observe that sputtering is the most extensively applied in the development of PGM coatings owing to its simplicity and flexibility to offer a broad range of material deposition.

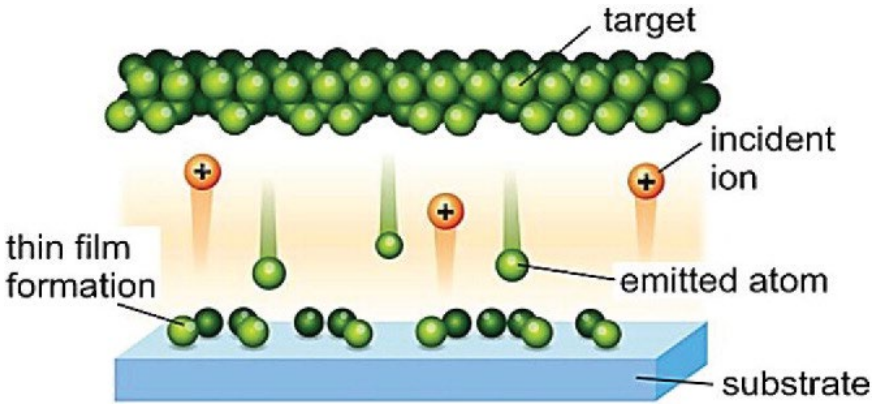

Figure 2. Illustration of sputtering procedure on an atomic scale [29]

2.1.2 Electron beam evaporation

An intensive electron beam (e-beam), produced from a filament and driven by both magnetic and electric fields, can also vaporize a target material in a vacuum (Fig. 3). Even materials with high melting points (e.g., metal oxides) can be effectively vaporized with e-beams [30]. E-beam evaporation is a rapid process with deposition rates of several micrometers per second, although the quality and adhesion of the developed film on a substrate may suffer from the low energy of the vaporized particles. Therefore, more sophisticated evaporation methods utilize excess plasma. The vaporized particles passing through the plasma region ionize, consequently, they can be accelerated to produce a film [31] denser than the columnar grains resulting from the conventional e-beam deposition because high-energy ionized particles can disrupt columnar growth. Thin films developed by this technique are of high quality and purity [32].

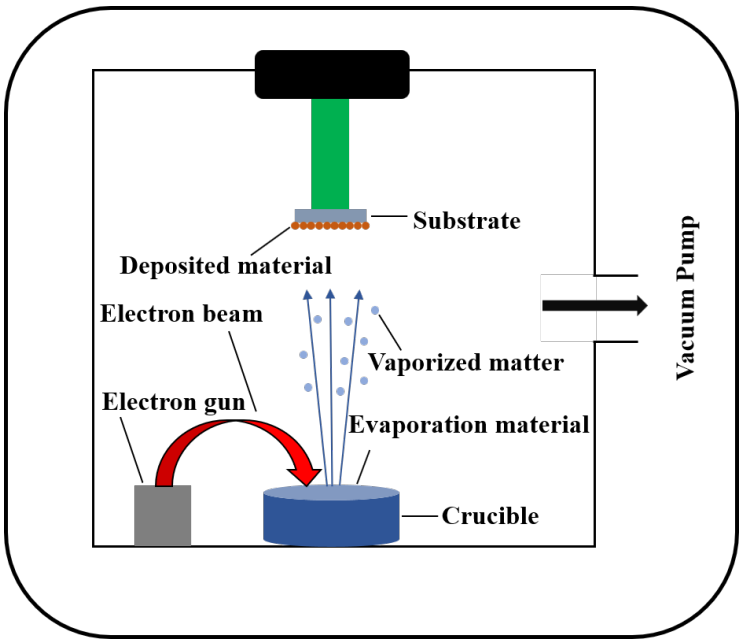

Figure 3. Schematic of e-beam evaporation [33]

2.1.3 Ion beam deposition

Similar to e-beam evaporation, energetic ions ejected from an ion source can also sputter material off a target, which, after plume formation, is deposited onto the substrate surface. A schematic of the ion beam deposition (IBD) is shown in Fig. 4(a). Technically, the significance of IBD is the controllability of ionic energies and the impact of ion occurrence on a developing surface. An additional ion gun can be utilized to assist deposition through bombardment with a developing film, called ion-beam assisted deposition (IBAD). Dual ionic beams facilitate stoichiometry control in thin films [34]. In addition, the bombardment of ions eliminates the

columnar microstructure (which is commonly observed in low-temperature PVD) to establish very dense and adherent films.

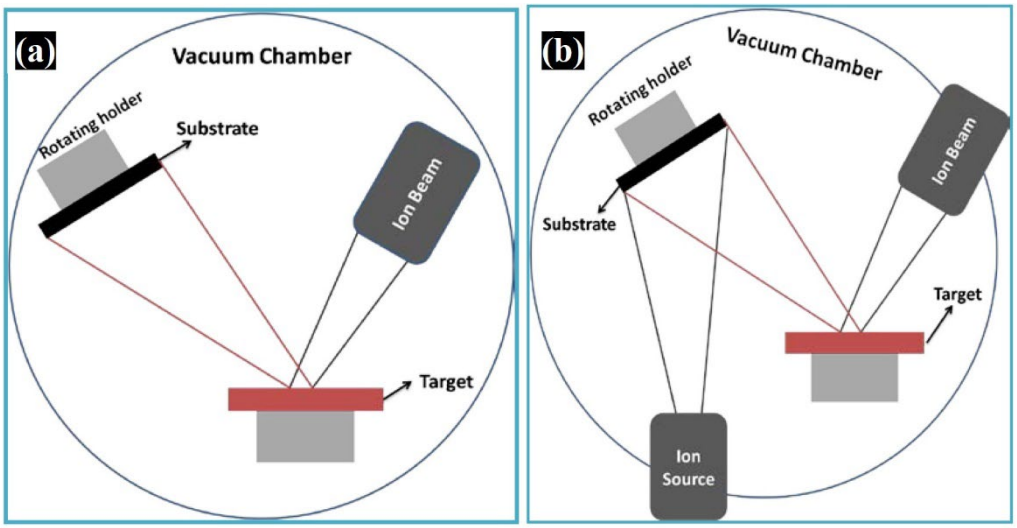

Figure 4. Schematic of (a) IBD and (b) IBAD [35]

2.2 Chemical vapor deposition

CVD is a general term for preparing thin films through a series of chemical reactions. In CVD, the material synthesis process occurs when the target constituents in the vaporized state react near the surface or into the substrate surface, resulting in film growth [36]. Various factors of this process are responsible for film quality, such as temperature, pressure, flow rate, and reactor geometry [37, 38]. The main distinctive features of CVD are its resourcefulness in producing either simple or complex compounds with comparative ease in terms of frequently low temperature, outstanding throwing power, uniform coating thickness, high growth rate, and the simplicity of epitaxial growth. CVD can be used to deposit materials that are difficult to vaporize, and it is more adaptable to depositing on substrates of complex shapes than other deposition techniques [24, 39]. Major CVD techniques include plasma-enhanced atomic layer deposition (PEALD), plasma-enhanced CVD, and metal-organic CVD.

Table 1 Deposition of coatings for PGM applications

Reference (Year)	Coating material / Interlayer	Substrate	Deposition technique [a]	Annealing temperature (°C)	Glass type	Major findings
Wu et al. [40] (2003)	PtIr, IrRe, IrReCrN /-	WC	RF-M.S.	500 °C	-	Thermal stability of the Ir-based coatings was observed at 500 °C
Lin et al. [41] (2006)	CrN, CrWN / -	Si, WC	IBAD	750 °C	-	Cr_2O_3 formation caused the increase in surface roughness of coatings and higher content of W in CrWN coatings demonstrated improvement in hardness
Chen et al. [42] (2006)	MoRu / Ni	WC	DC-M.S.	600 °C	-	Adequate thermal stability under 600 °C was observed w.r.t hardness and surface roughness
Kang et al. [9] (2007)	MoRu / Ni	WC	DC-M.S.	550 °C	-	An increase in surface roughness of the coatings was observed with an increase in interlayer (Ni) thickness and a decrease in hardness with a decrease in Mo content at 550 °C
Wen et al. [43] (2008)	NiRu /-	Si wafer	E.B.E.	600 °C	-	Substantial reduction in hardness at 600 °C was observed owing to the breakdown of the periodical multilayer structure
Chen et al. [44] (2009)	MoRu / Cr, Ti(O)	WC	RF-M.S.	600 °C	-	Better oxidation resistance and higher hardness with the increase in Ru content were observed at 600 °C
Chien et al. [45] (2010)	PtIr / TaN	WC/Co	M.S.	700 °C	L-BAL42	Restriction of WC/Co diffusion with the TaN interlayer was observed
Bobzin et al. [46] (2010)	PtIr / Ni, Cr	WC	PVD	-	-	Evaluation of the protective coatings via a nanoimpact test revealed the better adhesion property with Cr interlayer than Ni interlayer
Sakurai et al. [47] (2010)	PtZrNi / -	WC	RF-M.S.	450 °C	BK7	An increase in Zr content in PtZrNi coatings deteriorated the anti-sticking performance
Fischbach et al. [48] (2010)	PtIr, TiAlN / Ni	WC, Si	DC-M.S.	550 °C	P-SK57	Superior anti-sticking performance was observed with PtIr coating than TiAlN coating in actual PGM condition

Masuda et al. [49] (2011)	PtIr, IrRe / Ni	Steel	RF-M.S.	570 °C	-	Faster Ni diffusion in PtIr coating was observed than in IrRe coating after heat treatment at the same temperatures
Chen et al. [50] (2011)	TaN / -	WC-Co	DC-M.S.	500–800 °C	-	Diffusion of oxygen occurred through the columnar structure of the annealed TaN_x coatings above 500 °C, making the TaN-based coatings unapplicable for PGM
Tseng et al. [51] (2011)	PtIr, NiIr / Cr	WC	ISAMSS	700 °C	L-LAH83, N-KZFS5, K-LaK8	Less oxidation resistance with NiIr coating than PtIr coating at 700 °C
Klocke et al. [52] (2011)	PtIr / Ni, Cr	WC	PVD	-	-	Improvement in adhesion and effective strength with either Ni or Cr interlayer (Cr interlayer is relatively more effective)
Bobzin et al. [53] (2012)	PtIr / Cr	WC/Co	MSIP-PVD	650 °C	P-LASF47, N-FK5	Diffusion of Cr interlayer was observed into the PtIr coating, increased glass defects at the glass–coating contact zone with the increase in interlayer thickness
Lin et al. [54] (2013)	CrWN / -	Si, WC	M.S.	500 °C	K-PG325	CrWN coatings demonstrated improved anti-sticking with glass at 400 °C
Chao et al. [14] (2013)	PtIr / Ta	WC/Co	M.S.	596–607 °C	N-PK, N-FK, P-SK, L-NB, N-PS	PtIr coating displayed enhanced anti-sticking performance for different optical glasses.
Liu et al. [55] (2013)	ReIr / -	Si	M.S.	600 °C	-	The annealed ReIr coating with increased Ir content exhibited better thermal stability at 600 °C
Bobzin et al. [17] (2014)	PtIr / Ni, Cr	WC/Co	M.S.	590–645 °C	L-BAL42, P-LASF47, N-FK5	Severer interfacial reaction between coating and glass with an increase in Co content in the substrate
Chen et al. [56] (2014)	TaSiN / -	Si	DC-M.S.	600 °C	-	The preferential oxidation of Si occurred in TaSiN coatings. During 600 °C annealing, the inward diffusion of oxygen was restricted by the development of Si oxide scales.
Chen et al. [57] (2014)	TaN, CrTaN, TaSiN, CrTaSiN / -	Si wafer	M.S.	600 °C	BK7	Thermal stability of as-deposited Ta-nitride coatings (TaN, CrTaN, TaSiN, CrTaSiN) after cyclic annealing

						were evaluated. CrTaSiN demonstrated the best mechanical properties with the lowest roughness, making it a suitable candidate for glass molding.
Chen et al.[58] (2014)	CrTaSiN / -	Si, WC	M.S.	600 °C	SiO_2-ZnO-La_2O_3 and SiO_2-B_2O_3-BaO glasses	Increased nanohardness was observed for CrTaSiN coatings in comparison with Cr-free coatings and outward diffusion of glass elements (Ca, Na, Zn) during thermal cycling resulted in the reduction of coatings (CrTaSiN) surface quality.
Zhu et al.[59] (2015)	ReIr / Ta	WC/Co	RF-M.S.	631 °C	D-ZK3	The Re/Ir multilayer exhibited better anti-stick performance than Re and Ir monolayers for barium crown optical glass.
Chen et al.[60] (2015)	CrWN / Cr	Si, WC	DC-M.S.	600 °C	SiO_2-B_2O_3-BaO-based glass	Higher W content resulted in the reduction of nano hardness at 600 °C, owing to WO_3 formation.
Klocke et al.[61] (2016)	PtIr / Ni	WC	M.S.	640 °C	B270	Selective oxidation of Ni was occurred owing to the grain boundary diffusion.
Peng et al.[62] (2017)	PtIr / Cr, Ni	WC	M.S.	630 °C	-	Outward diffusion phenomena were observed for Ni and Cr interlayer owing to grain boundary segregation in which Ni diffusion is faster than that of Cr.
Chang et al.[63] (2018)	ZrSiN / Ti	Si, WC	DC-M.S.	600 °C	SiO_2-B_2O_3-BaO based glass	ZrSiN coatings with higher Si contents (>30 at. %) exhibited an amorphous phase with increased hardness, which was ascribed to the variation in the bonding characteristics.
Lee et al.[64] (2018)	AlCrN / -	WC	M.S.	800–900 °C	-	The atomic ratio of Al/Cr was nonuniform, causing a detrimental effect on the oxidation resistance at higher temperatures.
Wei et al. [65] (2019)	ReIr / Ta	WC	M.S.	631 °C	D-ZK3	Enhancement in mechanical performances and restriction of atomic diffusion were observed with a Re/Ir multilayer compared with Re and Ir monolayers.

Friedrichs et al. [66] (2020)	PtIr / Cr	WC	DC-M.S.	640 °C	B270	PtIr coating surface deteriorates (increasing defects) with increased molding cycles.
Huang et al. [67] (2020)	CrWN / -	Si, WC	PEMS	650 °C	BK7	Severe oxidation of the annealed coatings occurred in air and the higher W content increased the surface roughness and coating thickness.
Chen et al. [68] (2020)	CrSiN, TaSiN, ZrSiN / Cr, Ti	WC	DC-M.S.	600 °C	SiO_2-B_2O_3-BaO-based glass	ZrSiN coatings exhibited better anti-sticking in glass molding than CrSiN and TiSiN coatings.
Zhang et al. [69] (2020)	α-Al_2O_3 / TiN	WC	CVD	280 °C, 540 °C	D-ZK3, IRG206	α-Al_2O_3 multilayer coatings developed using CVD exhibited better anti-sticking properties with D-ZK3 glass and chalcogenide glass compared with DLC coatings
Li et al. [70] (2020)	CrWN / -	WC	PEMS	650 °C	BK7	Increased W content resulted in the enhancement of Young's modulus and nanohardness and a decrease in the surface roughness.
Guo et al. [71] (2020)	CrWN / -	Si, WC	PEMS	650 °C	-	The as-deposited coatings exhibited the nonuniform distribution of the solid-solution matrix, whereas annealing caused homogenization, resulting in considerable age-hardening.

[a] RF-M.S.: radio frequency magnetron sputtering; DC-M.S.: direct current magnetron sputtering; E.B.E: Electron beam evaporation; PEALD: Plasma enhanced atomic layer deposition; PVD: Physical vapor deposition; M.S.: Magnetron sputtering; ISAMSS: Ion source assisted magnetron sputtering system; MSIP-PVD: magnetron sputter ion plating physical vapor deposition; PEMS: plasma-enhanced magnetron sputtering; IBAD: ion beam assisted deposition; CVD: chemical vapor deposition

3. Anti-sticking and durability

3.1 Overview of coating materials

Among the various coatings developed for PGM, as identified in several papers [40, 72], noble metal coatings are generally employed in industries because of their superior oxidation and corrosion resistance and better reliability than other coatings. Noble metals are nonreactive with cations, anions, and network atoms in glasses in the temperature range for PGM (typically 600 – 700 °C) [40]. Another advantage over other coatings is that the coating process for noble metals is simple, as an industrial sputtering facility can serve this purpose. Klocke et al. [73] compared nitride and noble metal coatings on tungsten carbide (WC) substrates and observed that noble metal coatings exhibited a significantly better resistance to oxidation and anti-sticking properties than nitride coatings at or below 700 °C. Another study by Tseng et al. [51] demonstrated that PtIr coatings have better mechanical properties than NiIr coatings on WC substrates. Fischbach et al. [48] compared PtIr and TiAlN coatings on WC and Si substates in industrial glass molding atmospheres and observed that PtIr coatings exhibited significantly better anti-sticking properties than TiAlN coatings. Table 1 shows the different coating types, substrate materials, interlayer materials, and deposition techniques that were employed in previous PGM applications. It is evident that the PtIr coating is the most widely adopted among the noble metal coatings, owing to its chemical inertness and anti-sticking property. Additionally, WC is extensively employed as a substrate material owing to its remarkable wear resistance and thermal stability, and nickel (Ni) or chromium (Cr) interlayers are the most applied to promote adhesion between the noble metal coatings and substrates, and PVD, in particular magnetron sputtering, is extensively applied to develop coatings. However, considering the high cost of noble metals and the further elevated PGM temperatures, efforts are still required to develop ceramic coatings or a combination of ceramic and metallic coatings. In the following section, we review the existing coatings and their performance in PGM applications.

3.2 Noble metal coatings

3.2.1 Anti-sticking property

In a PGM process, glass–mold sticking at molding temperatures is a critical problem that results in limitations in the quality of molded glass products and the lifetime of molds [59]. In addition, molding tools undergo cyclic thermomechanical and chemical loads. Therefore,

coatings are required to protect and improve the service lifespans of molding tools. Friedrichs et al. [66] investigated the glass adhesion properties of four different PtIr protective coatings on cemented WC substrates. Energy-dispersive X-ray spectroscopy (EDX or EDS) data obtained from scanning electron microscopy (SEM) of four different PtIr-coated samples with and without the Cr interlayer after multiple molding cycles are shown in Fig. 5. When there was no interlayer, several small regions of damage appeared on the coating surface. The corresponding EDX data revealed that adhesion occurred as a significant level of glass elements was identified on the surface. They observed that the degradation of the molding tool was due to the outward diffusion of W atoms. With the employment of a 20 nm Cr interlayer, glass adhesion was further reduced and the Cr oxide scale formed on the coating surface owing to the outward diffusion of Cr resulting in a roughness change and some glass adhesion. Comparing the interlayers of 20- and 5-nm Cr for 600-nm PtIr coatings, they observed that the thinner interlayer resulted in larger surface defects caused by glass adhesion. Tungsten (W) was identified in the adhesion areas, implying that before the deterioration of the Cr layer, substrate degradation occurred because of the outward diffusion and accumulation of W on the surface. Such a coating failure mechanism was further corroborated based on the result of thinner coatings, i.e., 300-nm PtIr and 20-nm Cr interlayer, which were rapidly damaged and spalled.

The study of Friedrichs et al. indicted the following challenges with the PtIr/Cr/WC system:

(i) Glass adhesion is primarily due to the diffusion of W and Cr towards the coating surface.

(ii) Selective oxidation of Cr after Cr atoms reach the surface causes an increase in surface roughness, which is the initial stage of degradation. This oxide scale impairs the anti-sticking performance, resulting in glass adhesion fragments on the surface. The internal consumption of Cr in the interlayer causes Kirkendall voids [62], which impairs PtIr coating adhesion.

(iii) In addition to the Cr oxide scale, glass adhesion also occurs in areas containing a large amount of W atoms emanating from the substrate. The existence of W resulted in more severe glass adhesion than the Cr oxide scale.

(iv) The service lifespans of coated WC-based molding tools, indicated by the extent of loss of anti-sticking performance, are governed primarily by the outward diffusion of W and secondarily by the diffusion of Cr.

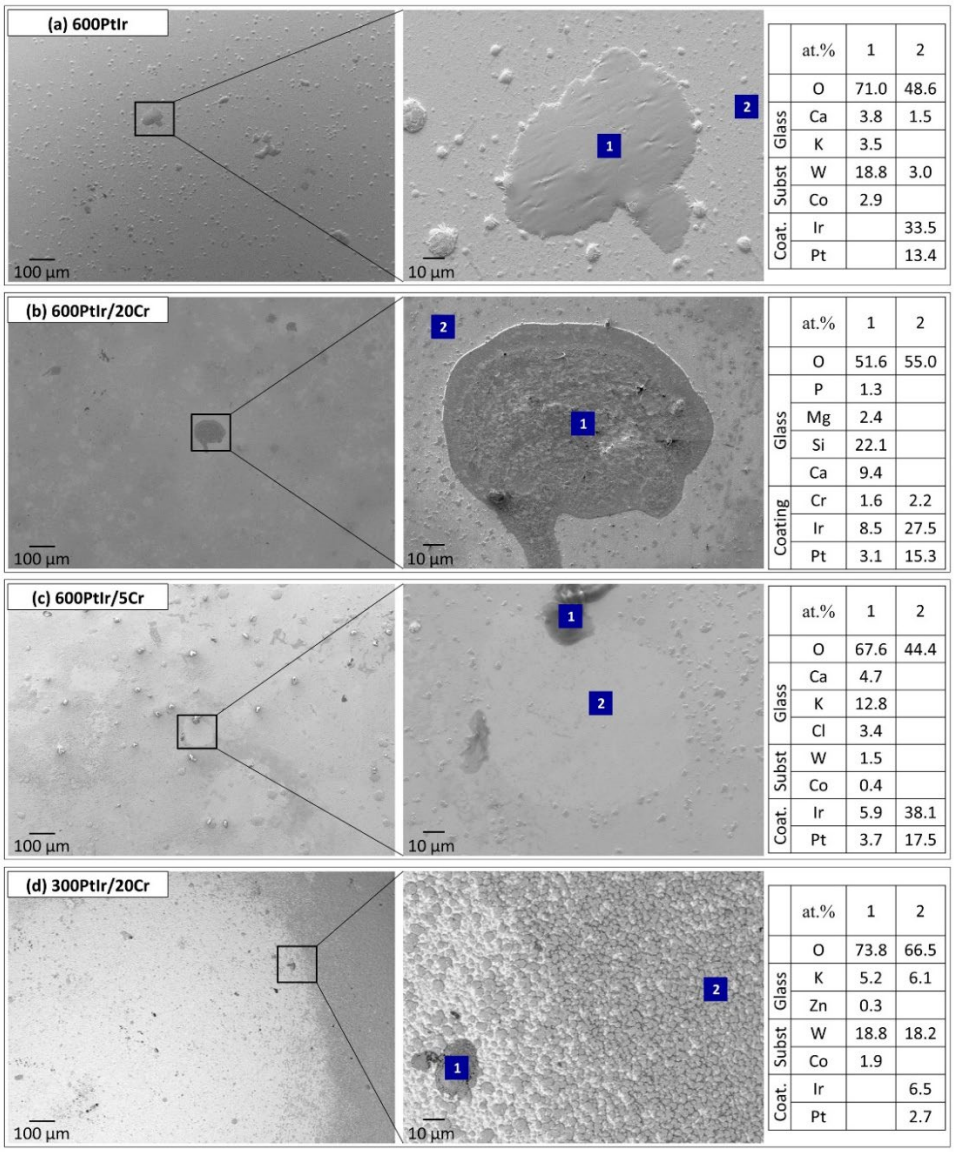

	at.%	1	2
	O	71.0	48.6
Glass	Ca	3.8	1.5
Glass	K	3.5	
Subst	W	18.8	3.0
Subst	Co	2.9	
Coat.	Ir		33.5
Coat.	Pt		13.4

	at.%	1	2
	O	51.6	55.0
Glass	P	1.3	
Glass	Mg	2.4	
Glass	Si	22.1	
Glass	Ca	9.4	
Coating	Cr	1.6	2.2
Coating	Ir	8.5	27.5
Coating	Pt	3.1	15.3

	at.%	1	2
	O	67.6	44.4
Glass	Ca	4.7	
Glass	K	12.8	
Glass	Cl	3.4	
Subst	W	1.5	
Subst	Co	0.4	
Coat.	Ir	5.9	38.1
Coat.	Pt	3.7	17.5

	at.%	1	2
	O	73.8	66.5
Glass	K	5.2	6.1
Glass	Zn	0.3	
Subst	W	18.8	18.2
Subst	Co	1.9	
Coat.	Ir		6.5
Coat.	Pt		2.7

Figure 5. SEM surface analysis and EDX data of four different PtIr coating systems [66].

Wei et al. [65] examined the anti-sticking property by applying the sessile drop technique (wetting test). In the wetting test, D-ZK3 glass balls were positioned on the coated substrates in a vacuum. The temperature was increased to 631 °C, 120 °C above the T_g, for one hour. Fig. 6 shows the wetting angle of the glass ball on the substrate with different coatings. They observed that at 631 °C, a slight adhesion occurred between the glass ball and both the Ir and Re coatings. Surprisingly, the Re/Ir multilayer coating resulted in minimum adhesion; the glass sample remained approximately spherical with a contact angle of 168.1°, significantly larger than those resulting from Re and Ir monolayers and WC (without coating). After the wetting test on the monolayer-coated samples, the surface of the glass ball became slightly opaque. High temperatures promoted inter-diffusion (or reactions) between the glass and coating. Moreover, the diffusion of active substrate elements towards the surface initiated the reaction,

resulting in a decrease in the wetting angle [74]. Conversely, the adherence of the optical glass ball with the substrate was reduced considerably after the multilayer Re and Ir coatings were developed, by which the glass ball remained fully transparent and no apparent sticking occurred after the wetting tests at 631 °C. Thus, a Re/Ir multilayer coating was suggested in [65]. Furthermore, this result indicated that multilayer coatings may be superior to monolayer coatings in terms of anti-sticking performance. For monolayers, diffusion is facilitated by grain boundaries [75, 76], whereas in multilayers [59, 77, 78], the interfaces of disparate elements enhance the resistance to diffusion, and therefore, better suppress the outward migration of substrate elements to react with the glass. Additionally, Refs. [79, 80] demonstrated that the ordered nanostructure resulted in higher resistance to the penetration of cations in glass (e.g., Ca, Ba) into the protective coatings, thereby facilitating the anti-sticking performance.

The primary function of protective coatings is to increase the lifespan of the mold by establishing a chemical barrier to prevent the most frequent failure, i.e., glass sticking. The above-mentioned studies indicated that at high temperatures in glass molding, the diffusion of active elements in the interlayer and substrate via the grain boundaries of the protective coatings towards the surface is the most common phenomenon that results in glass sticking. Therefore, the multilayer structure of noble metal coatings may bring about a notable improvement in anti-sticking performance, which is attributed to the impediment of atomic diffusion caused by the addition of interfaces.

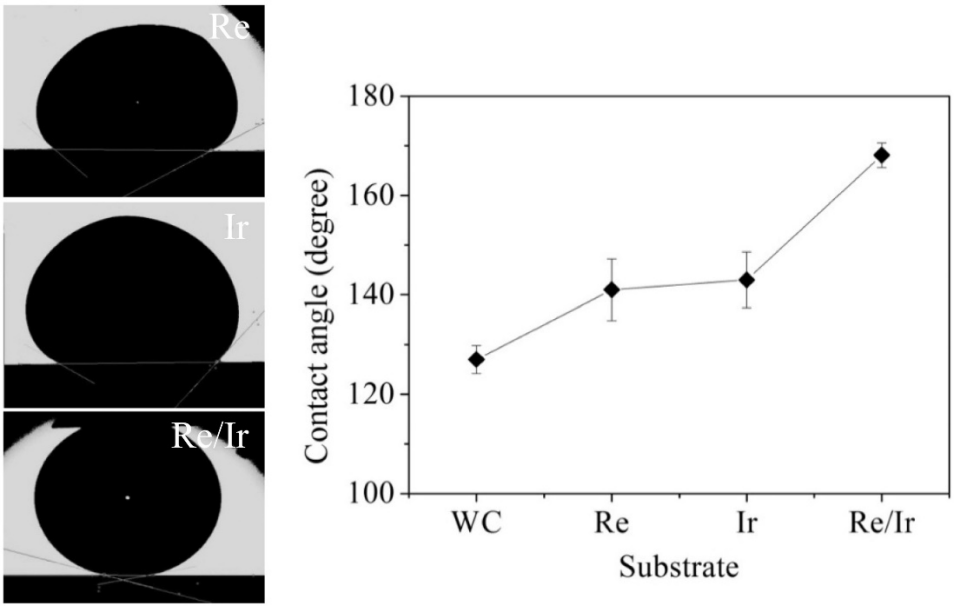

Figure 6. Wetting angle of different coatings at high temperatures [65]

3.2.2 Degradation mechanisms

PGM tools with protective coatings must undergo several hundred to thousand pressing cycles to justify their economic benefits over traditional material removal processes. This can result in changes in the surface topology, inertness, and even mechanical failure (e.g., spallation). Therefore, knowledge about the mechanism of coating failure is vital. Zirong et al. [62] examined the degradation mechanism of $Pt_{0.3}Ir_{0.7}$ coatings on WC substrates with Cr as the adhesive interlayer at 630 °C. The degradation evolution based on the experimental observations is depicted in Fig. 7. The outward transportation and segregation of Cr atoms along the grain boundaries of the protective coating was suggested as the leading degradation mechanism. From a thermodynamic perspective, diffusion is driven by chemical potential gradients and activities across the interfaces of disparate materials. However, grain boundaries provide fast channels, along which diffusion is a few orders of magnitude faster than within a grain [81]. Therefore, at a higher temperature of 630 °C and in a short period [82, 83], the outward transport of interlayer atoms occurs primarily through grain boundary diffusion, which forms oxide scales on the coating surface. The development of surface oxides is strongly influenced by the interior material transport. First, the decoration of solutes in PtIr grain boundaries is directed by the Gibbs adsorption isotherm, that is, the reduction in interfacial energy owing to the decoration of solutes. This results in a diffusion flux into the grain boundaries. When diffusive species arrive at the surface of the film, oxidation processes occur to eliminate the solutes, in particular, those from the decorated area at the grain boundaries owing to their trapping in the oxide scale. This impact results in the decrease in the solute chemical potential in the grain boundaries; thus, a chemical potential gradient towards the surface is established, which promotes further outward diffusion [84-89]. If the oxide scale is sufficiently dense to stop oxidation, the outward transport of the diffusive species can be slowed down [90].

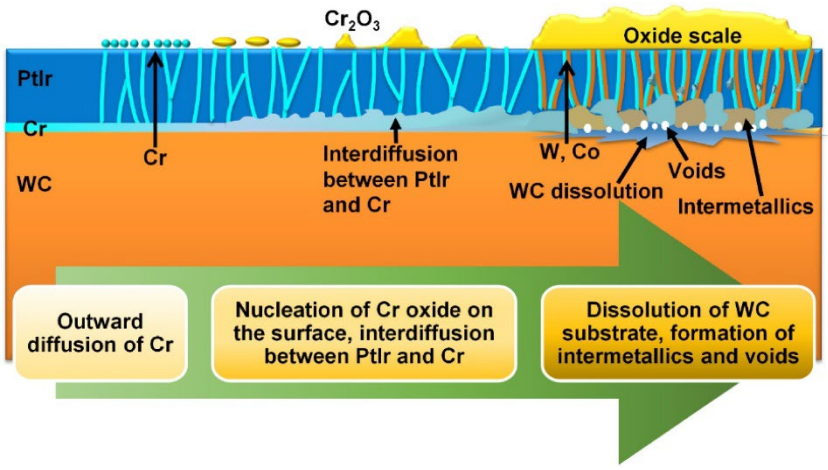

Figure 7. Illustration of degradation evolution mechanism of PtIr/Cr/WC at 630 °C [62]

Fig. 8 shows a three-dimensional element distribution of a heat-treated (at 630 °C) PtIr/Cr/WC system obtained using atom probe tomography. The appearance of Cr enrichment at both the grain boundaries of the protective coating and the interfacial areas are shown in Fig. 8(b) and 8(c), respectively. The diffusion of Cr results in the formation of intermetallic phases, which are initially Cr-rich compounds with a stoichiometry of $(Pt, Ir)_3Cr_2$ formed at the PtIr/Cr interfacial area. With continuous thermal exposure, the continuous consumption of the Cr interlayer is caused by the nuclei growth of such intermetallic compounds and oxide scale formation on the surface. When the Cr interlayer is fully consumed, the activity of Cr decreases, and the $(Pt,Ir)_3Cr_2$ formation stops. Subsequently, Cr atoms diffuse out from the intermetallic phase, resulting in the shrinkage of the $(Pt,Ir)_3Cr_2$ phase, which may change to the Cr-lean phase of $(Pt,Ir)_3Cr$ or completely vanishes. This phenomenon of second phase formation and depletion induced by supply limitation has also been observed in several previous studies [91-97].

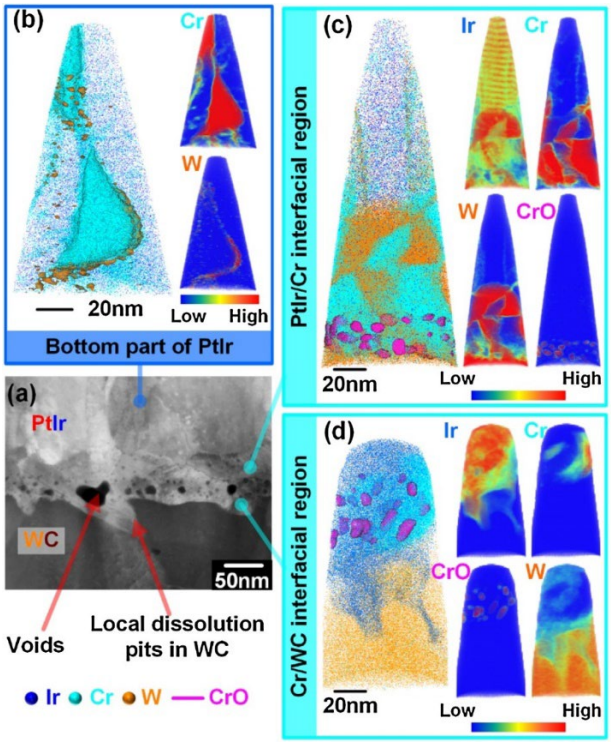

Figure 8. Typical characterization results acquired from the interfacial area of PtIr/Cr/WC specimen after heat-treatment at 630 °C: (a) STEM image and 3D atomic mappings of (b) PtIr layer bottom part, (c) PtIr/Cr interfacial area, and (d) Cr/WC interfacial area [62]

At the later stage of coating degradation, the involvement of the WC substrate in the diffusion process causes the development of W-enriched intermetallic compounds. Additionally, at the interfacial area, these intermetallic compounds form numerous voids,

known as the Kirkendall effect [98], in which imbalance mass transportation as a consequence of the difference in diffusion rates creates free volumes. During the outward diffusion of Cr-dominant species, vacancies drift in the opposite direction. These additional vacancies may condense into voids [99, 100], which play a crucial role in the commencement of WC degradation.

Klocke et al. [61] investigated the degradation of a PtIr coating with Ni as an adhesive interlayer. The PtIr-coated samples covered with B270 glass were heated at 640 °C for several heating cycles in a vacuum or nitrogen environment. The resulting coatings and glass are shown in Fig. 9(a). The marked regions in Fig. 9(a) were subjected to X-ray photoelectron spectroscopy (XPS) analysis, and the results are shown in Fig. 9(b). The study observed that Ni oxides formed only on the surface. At a depth of 20 nm, only metallic Ni was observed in the PtIr film. This demonstrated that external and selective oxidation occurred after the outward diffusion of Ni. Additionally, W and, to a smaller extent, cobalt (Co) oxides formed on the surface, indicating the oxidation of these species. The diffusion of nickel likely occurred through the grain boundary diffusion mechanism [49]. After sputtering to remove the 20 nm layer, nickel oxide was eliminated, and only metallic Ni was identified. An XPS analysis at a depth of 20 nm also demonstrated a considerable reduction in Co and W concentrations, which were significantly smaller than the Ni concentration. Therefore, it was hypothesized that the existence of Co and W on the surface is not the result of diffusion through the layers of PtIr and Ni. Instead, open craters were identified on the coating surface, where large fractions of W and Co were detected. The dimensions of the craters were 1–30 μm, suggesting that the PtIr/Ni layer was deformed and fractured by the media resulting from underneath, possibly because of the invasion of oxygen and the formation of W and Co oxides. Additionally, a high content of carbon was also identified using XPS analysis (zone 2); however, owing to the chemical inertness of carbon, it was not involved in glass adhesion with the surface [101, 102].

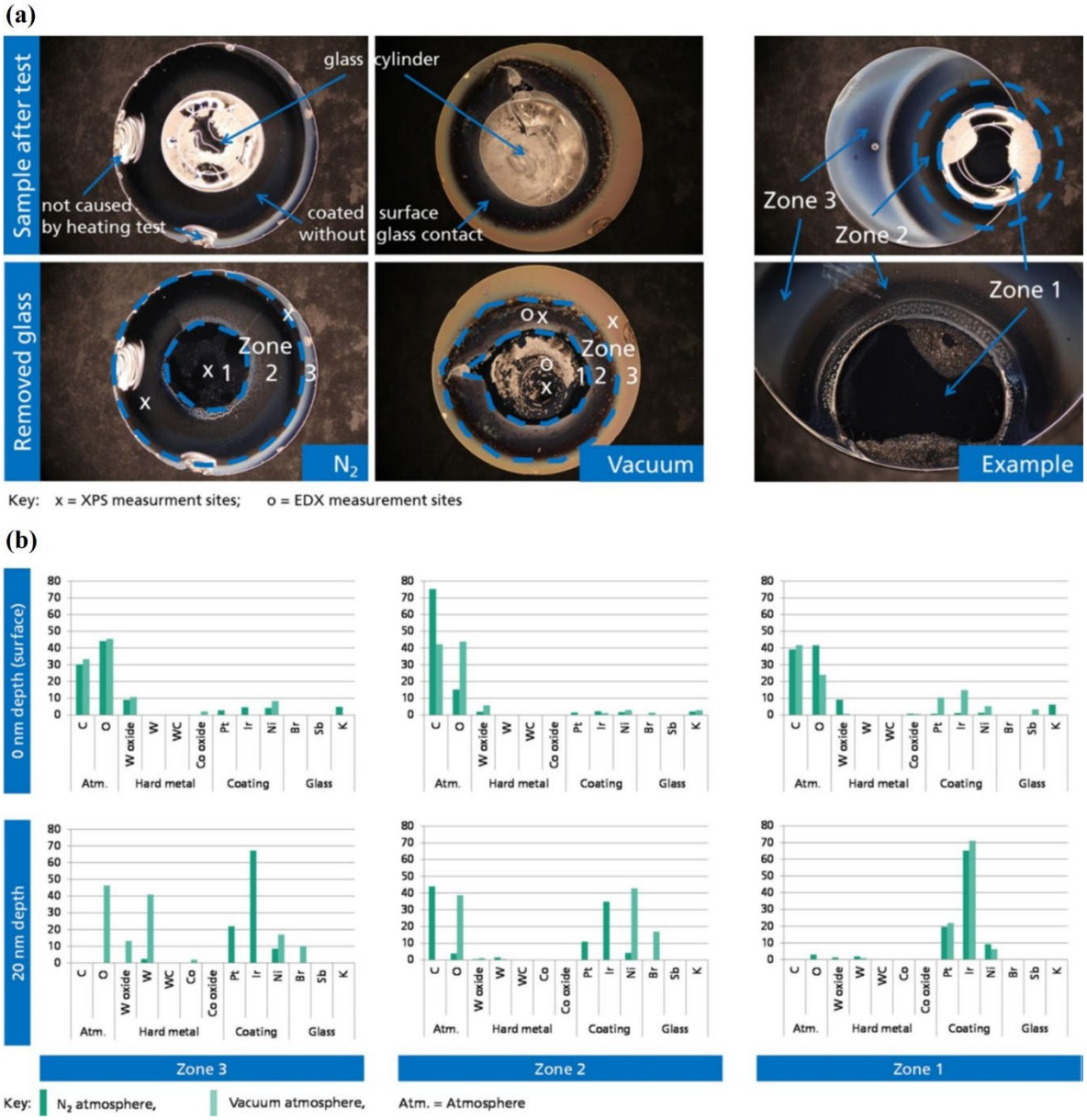

Figure 9. Evaluation of PtIr/Ni/WC: (a) optical images of specimens after heating tests with glass covers, and (b) XPS analysis of coating surfaces and subsurface [61]

Liu et al. [103] examined the chemical inertness of IrRe protective coatings developed on silicon (Si) substrates with B_2O_3-ZnO-L_2O_3 glasses in the temperature range of 270–600 °C. The results revealed that the invasion of Zn from the glass reduced the coating performance. Additionally, the formation of Zn compounds on the coating surface resulted in a significant increase in the surface roughness. In another study [49], IrRe and PtIr coatings were employed on Ni-P molds, and the results indicated that the diffusion of Ni was promoted in the grain boundaries of Ni and Ni_3P intermetallic in the plating structure towards the coating surface. However, Ni diffusion was suppressed in the IrRe coating owing to the smaller diffusion

coefficient of Ni in the IrRe alloy than in the PtIr alloy. MoRu coatings deposited on WC substrates have exhibited significant thermal stability in terms of surface characteristics and phase evolution, including hardness and roughness, after annealing at 600 °C [42]. Chen et al.[104] studied the annealing effect (at 600 °C) of TaRu and MoRu coatings in an oxygen-containing environment. They observed that the preferential internal oxidation phenomena occurred for tantalum (Ta) and molybdenum (Mo) in the coatings; however, the ruthenium (Ru) element remained in its metallic state. Owing to internal oxidation, the resulting laminated oxide structures converted TaRu and MoRu coatings into alternating layers of (Ta_2O_5, Ru) and (MoO_2, Ru), respectively.

Above studies have shown that the degradation of coated molds is primarily influenced by the interfacial areas of interlayers with protective (noble metal) coatings and with substrate. Owing to thermal instability, outward movement and segregation of the interlayer material along the grain boundaries of the protective coatings appears to be the beginning of the degradation process at glass-molding temperatures. In addition, the creation of voids at the interlayer/substrate interface owing to the departure of interlayer materials results in the weakening of coating-substrate adhesion as well as the outward diffusion of substrate materials. As the service lifespan of the coated molds is vital to PGM application, further research is suggested to focus on quantitative modelling of the above degradation mechanisms to predict the lifespan of coated models for given coating structure and molding temperature.

3.2.3 Ruthenium as a metal coating

Ru, which is a cost-effective noble metal, has gained interest because its oxidation resistance is even higher than that of other noble metals, such as platinum (Pt) and iridium (Ir) [105]. Chen et al. [44] employed MoRu coatings on WC substrates; after annealing at 600 °C, they observed that coatings with high Ru content (at least higher than Mo content) exhibited superior oxidation resistance and higher hardness. Their results indicated that Ru is a suitable coating material for high-temperature applications. Ru has been used as a metallic film for contact switching in microelectromechanical systems (MEMS) with enhanced mechanical properties compared to Pt, gold (Au), rhodium (Rh), and silver (Ag) [106]. Although Ru, along with Pt, primarily appears as an electrocatalyst in the literature [107], owing to its higher oxidation resistance, it can be a coating material for PGM when an increase in chemical inertness is required, specifically when high-T_g glasses are subjected to molding.

Han et al.[108] deposited Ru thin films on Si substrates using pulsed CVD and ALD with the same thickness to compare the thermal stability of the surface characteristics before and after thermal annealing (Fig 10). The surface roughness and morphology were examined using

atomic force microscopy (AFM). Fig. 10(a) shows the variation in roughness with rapid thermal annealing (RTA). In the as-deposited state, Ru thin films grown using pulsed CVD exhibited a smaller roughness than those grown by ALD owing to the smaller grain size. The AFM images of the annealed state (Fig. 10(b)) indicated that the small roughness of the CVD Ru films was maintained up to a high temperature of 800 °C, whereas the ALD Ru films had a significant increase in the roughness. In addition, ALD Ru films demonstrated void formation owing to the excessive growth of grains, whereas a minor increase in grain size was observed for CVD Ru films. These results clearly indicated that CVD Ru films have higher thermal stability than ALD Ru films.

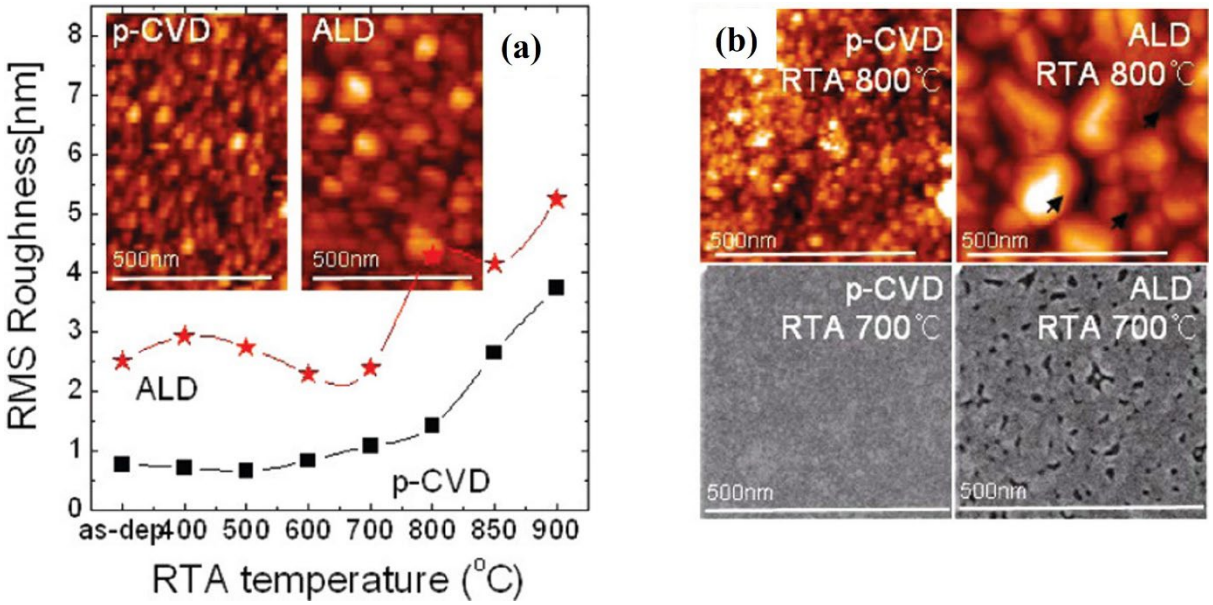

Figure 10. (a) Roughness comparison of Ru films deposited using p-CVD and ALD (inset AFM images), and (b) AFM images (upper part) at 800 °C and SEM images (lower part) at 700 °C of Ru films [108]

Chen et al. [109] developed TaRu coatings on WC substrates with a Cr interlayer using DC magnetron co-sputtering. Four alloy coatings ($Ta_{35}Ru_{65}$, $Ta_{45}Ru_{55}$, $Ta_{55}Ru_{45}$, $Ta_{64}Ru_{36}$) were achieved with pure metal targets (Ta, Ru, Cr) at 400 °C. To investigate the stability of TaRu coatings, they annealed the coatings in an oxygen-containing environment at 600 °C for 4 h and then cooled them to room temperature. Fig. 11 shows the XRD, SEM, and TEM analyses of the as-deposited and annealed TaRu coatings. In the as-deposited state, the XRD patterns revealed the reflections of hexagonal Ru, tetragonal β-Ta, and hexagonal RuTa (Fig. 11(a)), whereas the annealed coatings exhibited reflections of Ru, RuTa, and Ta_2O_5, indicating the oxidation of tantalum at 600 °C. The cross-sectional SEM images demonstrated the columnar morphology of the TaRu coatings on the substrate and the formation of an oxide scale on the top surface of the coatings after annealing. The developed TaRu coatings with a

relatively higher Ru content exhibited fewer thickness changes after annealing. With the minimum amount of Ru, the overall thickness of the coating $Ta_{64}Ru_{36}$ increased from 702 to 740 nm due to oxidation, which resulted in a layered structure (Fig. 11(e)). Because the $Ta_{64}Ru_{36}$ coating was annealed in an oxygen environment, the inward oxygen diffusion was faster than the outward Ta diffusion. In addition, Ta formed an oxide more easily than Ru, resulting in internal oxidation [110, 111].

Chen et al. [112] fabricated CrRu protective coatings using magnetron co-sputtering with Ti as an interlayer on Si substrates. The CrRu coatings were deposited at 400 °C and then annealed in a 50 ppm O_2-N_2 environment for 2 h at 600 °C. Fig. 12 shows the cross-sectional microstructural behavior of the $Cr_{47}Ru_{53}$ and $Cr_{65}Ru_{35}$ coatings in the as-deposited and annealed state. After co-sputtering, $Cr_{47}Ru_{53}$ and $Cr_{65}Ru_{35}$ exhibited compact polycrystalline morphologies and columnar structures, respectively. After annealing, thick oxide scales formed on the surfaces of both co-sputtered coatings and the columnar structure transformed into a polycrystalline structure in the $Cr_{65}Ru_{35}$ coating. The size of the recrystallized grains was limited by the original columnar grain boundaries, resulting in smaller grains in the $Cr_{65}Ru_{35}$ coating than in $Cr_{47}Ru_{53}$. The electron diffraction patterns indicated that the CrRu and oxide scale regions consisted of Ru-based alloys and Cr_2O_3, respectively.

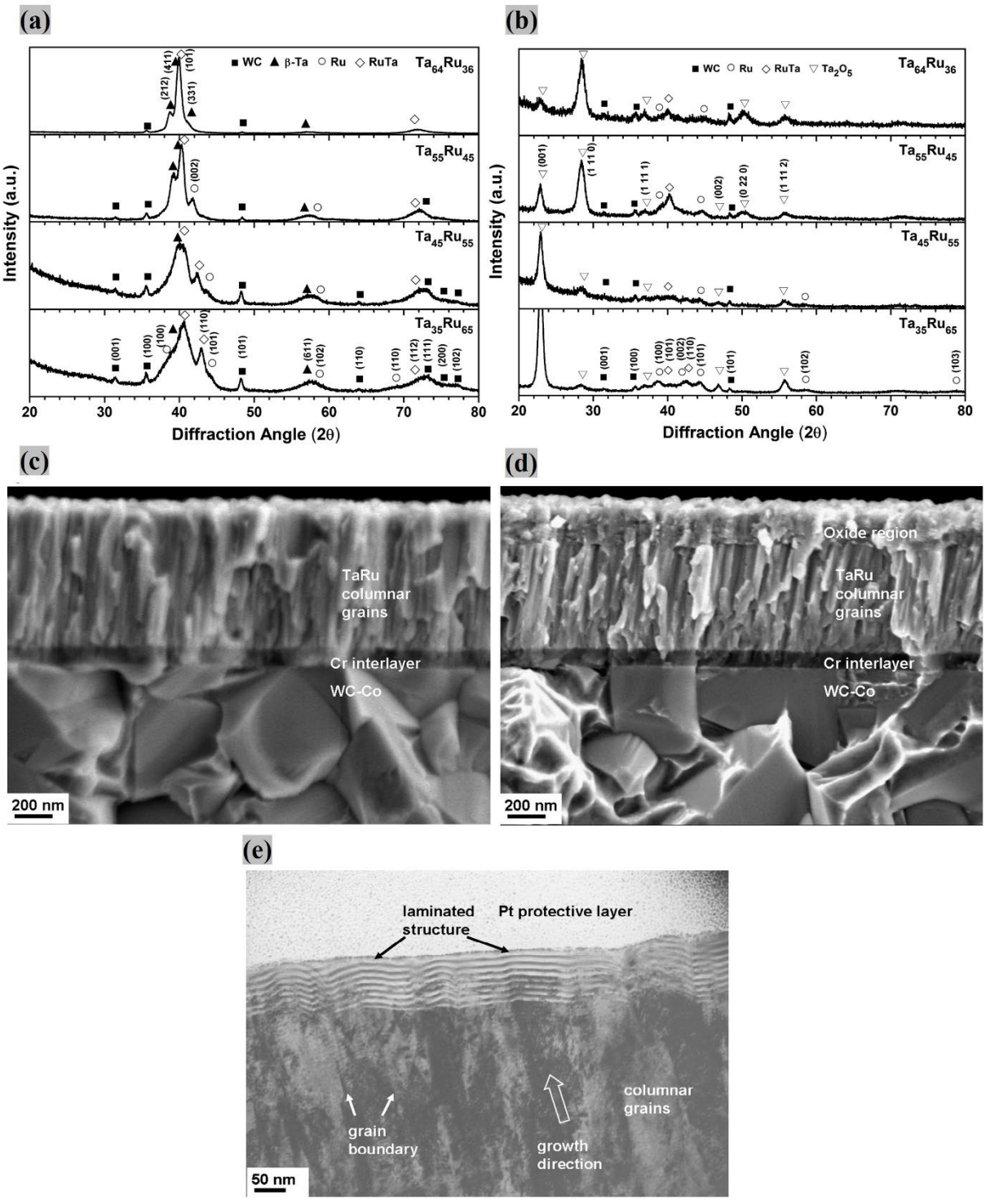

Figure 11. Study of $Ta_{64}Ru_{36}$ coatings: XRD patterns of the (a) as-deposited and (b) annealed coatings, cross-sectional SEM images of the (c) as-deposited and (d) annealed coatings, and (e) cross-sectional TEM image of the annealed coatings [109]

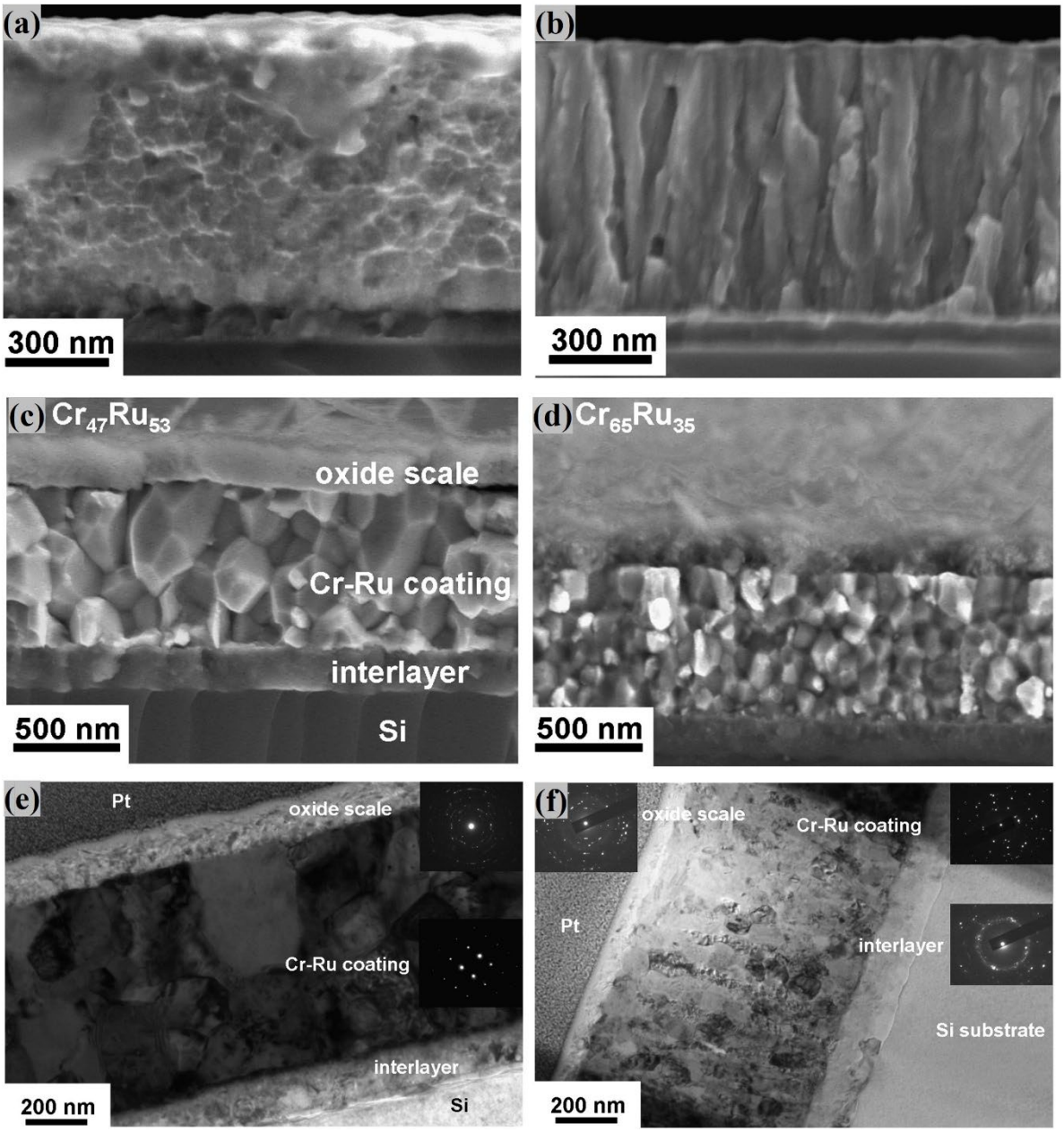

Figure 12. Study of $Cr_{47}Ru_{53}$ and $Cr_{65}Ru_{35}$ coatings characterized by cross-sectional SEM images of (a, b) as-deposited and (c, d) annealed coatings, and cross-sectional TEM images of (e, f) annealed coatings [112]

3.3 Ceramic coatings

While noble metal coatings are more advantageous than ceramic ones in prolonging the lifetime of PGM tools, the research on ceramic coatings has not stopped because of the lower cost that can potentially achieve a better combination of cost and durability, particularly when higher temperatures in PGM are required. Li et al. [70] fabricated CrWN ($Cr_{35}W_{18}N_{47}$, $Cr_{27}W_{24}N_{49}$, $Cr_{18}W_{28}N_{54}$, and $Cr_{13}W_{31}N_{56}$) coatings on WC substrates using co-sputtering Cr and W targets in a plasma sputtering system. The coating surfaces were analyzed using AFM

before and after the pressing cycles of glass molding at a maximum temperature of 650 °C. As the W content increased, finer particle sizes and decreased surface roughness of the CrWN coatings were observed. The addition of W to CrN resulted in the formation of a dense and fine-grained structure of the coatings because the addition of W atoms in co-sputtering caused an enhancement in the collision of Cr and N. Additionally, mobility and diffusivity could be restrained by the higher W content. Previous studies [113, 114] reported that the increase in the energy of the (sputtering) W target caused a decrease in the surface roughness of the coatings. For the $Cr_{35}W_{18}N_{47}$ coating, the maximum and minimum particle sizes were 337 and 107 nm, respectively. In addition, the formation of finer particles occurred in other coatings ($Cr_{27}W_{24}N_{49}$, $Cr_{18}W_{28}N_{54}$, and $Cr_{13}W_{31}N_{56}$) if the W target power was increased. Fig. 13 shows the surface morphology of the $Cr_{35}W_{18}N_{47}$ coating before and after thermal pressing cycles in a nitrogen environment. The surface roughness of the $Cr_{35}W_{18}N_{47}$ coating in the contact region with glass (Fig. 13(h)) and noncontact region (Fig. 13(i)) were 12.3 and 14.6 nm, respectively. The increase in the surface roughness of the noncontact region, associated with cracks, was caused by oxidation at high temperatures. The same phenomena were also observed for other coatings ($Cr_{27}W_{24}N_{49}$, $Cr_{18}W_{28}N_{54}$, and $Cr_{13}W_{31}N_{56}$). The extent of oxidation in the contact regions was relatively small because the cover glass inhibited the oxygen accessibility. Huang et al. [67] synthesized CrWN coatings with varying W contents using magnetron sputtering and examined the molding performance of the coatings in a nitrogen environment at 650 °C for 6 min. The fabricated coatings with varying W contents were $Cr_{34.45}W_{20.94}N_{44.61}$, $Cr_{28.03}W_{33.29}N_{38.68}$, $Cr_{18.90}W_{40.13}N_{40.97}$, and $Cr_{15.73}W_{44.94}N_{39.33}$. In the $Cr_{34.45}W_{20.94}N_{44.61}$ coating, with a low W content, a coarse granular morphology was observed with many noticeable micro-sized pores. Although the deposition techniques were different, the effects of W content were the same as those revealed by Li et al. [70], that is, the increase in W content results in grain refinement and a smoother surface, but it aggravates oxidation.

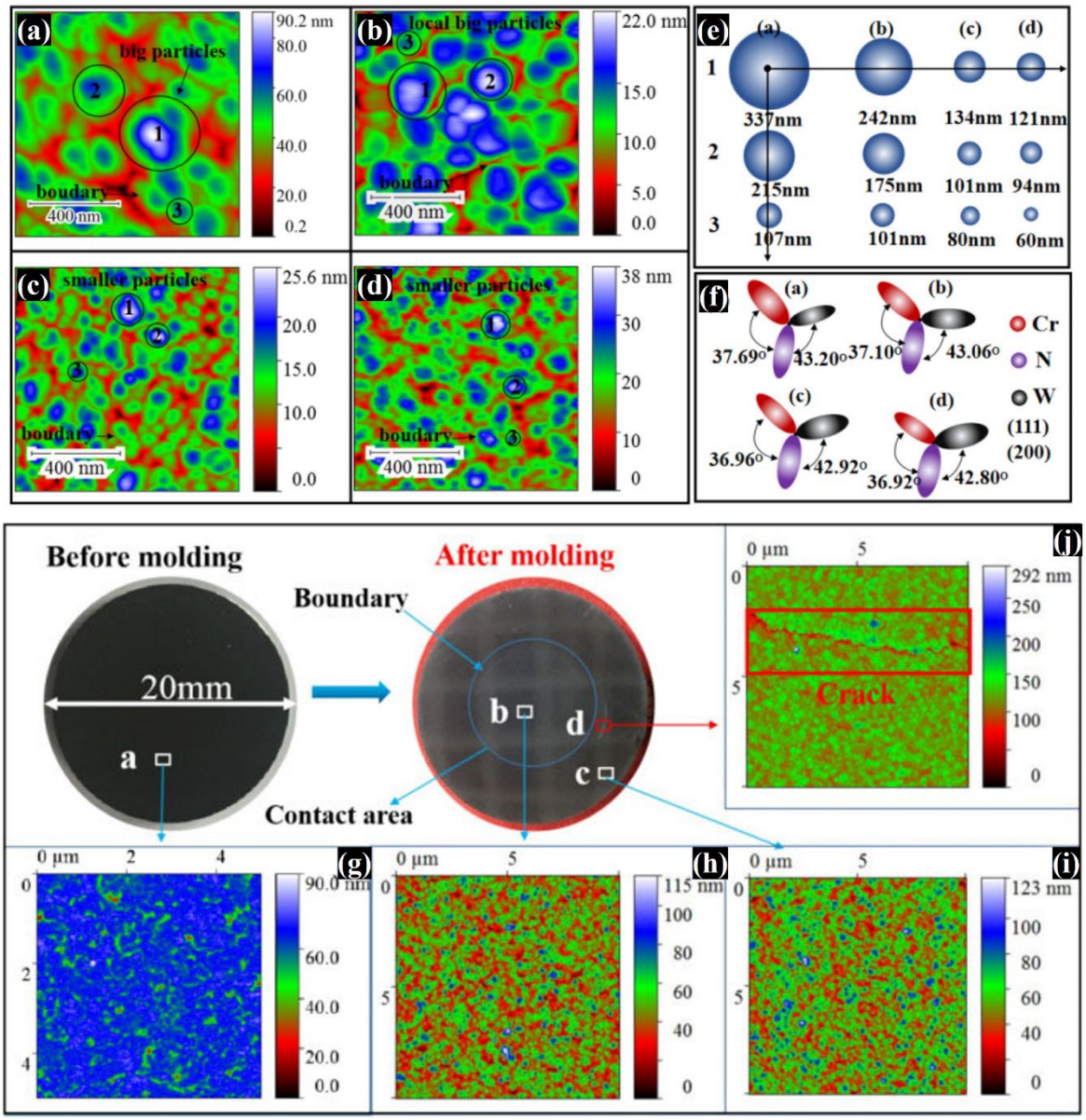

Figure 13. AFM study of CrWN coatings: (a–d) surface morphologies of as-deposited ($Cr_{35}W_{18}N_{47}$, $Cr_{27}W_{24}N_{49}$, $Cr_{18}W_{28}N_{54}$, and $Cr_{13}W_{31}N_{56}$) coatings, respectively, (g–j) surface morphology of annealed $Cr_{35}W_{18}N_{47}$ coating [70]

Li et al. [70] schematically revealed the degradation mechanism of CrWN coatings (Fig. 14). At the molding temperature in the PGM, the top surface of the coatings experienced high pressure. As the number of thermal cycles increased, the columnar voids of the coated structure provided diffusion channels for oxygen. In addition to the formation of surface oxide layers, internal oxidation also occurred. The aggravation of W and Cr oxidation significantly reduced the integrity of the coatings. The anti-adhesion and mechanical properties decreased abruptly, and cracks were observed owing to the interfacial reaction, sticking, and oxidation. With the increase in thermo-mechanical cycles, the cracked coatings eventually fell off owing to the sticking and demolding forces.

Chen et al. [56] prepared TaSiN coatings via magnetron co-sputtering on Si substrates. The cross-sectional TEM images of the coating before and after annealing at 600 °C are shown in Fig. 15. The selected-area diffraction pattern (SADP) demonstrated a noncrystalline phase. The HRTEM image revealed the stacking of the coating constitution with periodic gradient concentration; however, the lattice fringes were not identified. In the annealed state, the $Ta_{27}Si_{20}N_{53}$ coating exhibited an oxide scale formed on the surface. Underneath the oxide scale, the amorphous structure of the coatings was maintained (inset of Fig. 15(c)). The oxide scale continued to expand during prolonged heating and remained amorphous, whereas the internal part of the coating demonstrated crystalline domains embedded in the amorphous matrix. The crystalline domains were identified based on the apparent lattice fringes attributed to the Ta_2N and TaN phases.

Chen et al. [68] further investigated the chemical inertness of silicon-nitride-based ($Cr_{28}Si_{17}N_{55}$, $Ta_{26}Si_{14}N_{60}$, $Zr_{16}Si_{20}N_{64}$) coatings in contact with SiO_2-B_2O_3-BaO glass at temperatures between 270 and 600 °C (Fig. 16). For the $Cr_{28}Si_{17}N_{55}$ coatings, significant glass adhesion was observed after the first ten thermal cycles. After 100 thermal cycles, the optical microscopy (OM) and SEM images revealed a damaged surface, indicating adhesiveness with glass. The WC substrate underneath was exposed, which was also confirmed using EDS analysis. After 400 thermal cycles in the $Ta_{26}Si_{14}N_{60}$ coatings, the contact region of the coating with glass became opaque (the as-deposited coatings were transparent), possibly because of the formation of oxide islands with a maximum diameter of 200 nm, as observed in the contact region. Moreover, the original granular morphology was maintained in the noncontact region. After 600 thermal cycles, the TEM image (Fig. 16(f)) of the $Ta_{26}Si_{14}N_{60}$ coatings revealed the formation of an oxide scale on the coating surface and the expansion of the interlayer area. Based on the EDS analysis of the surface oxide, no identification of Ti was observed, which indicated that the $Ta_{26}Si_{14}N_{60}$/Ti/WC coating restricted the outward diffusion of Ti. After being heated for 400 cycles, the $Zr_{16}Si_{20}N_{64}$ coatings became translucent, i.e., the granular morphology underneath the coatings could be partially observed. This was because the island oxides were smaller (~20 nm) than those in the heated $Ta_{26}Si_{14}N_{60}$ coatings. With continued annealing after 600 and 800 thermal cycles, the oxide particles further expanded to 20–40 nm and 150 nm, respectively (Fig. 16(h) and 16(i), respectively). The elemental mapping of the $Ta_{26}Si_{14}N_{60}$ coatings in the contact region indicated that the oxide particles had high amounts of Ba and O with low levels of N and Zr. These results indicated that the $Zr_{16}Si_{20}N_{64}$ coatings demonstrated better chemical inertness than $Cr_{28}Si_{17}N_{55}$ and $Ta_{26}Si_{14}N_{60}$ against BK7 optical

glass. Chang et al. [63] also studied the oxidation resistance of ZrSiN coatings at 600 °C. Their results indicated that the improved oxidation resistance was attributed to the formation of dense Zr-Si-O oxide scales that inhibited oxygen diffusion.

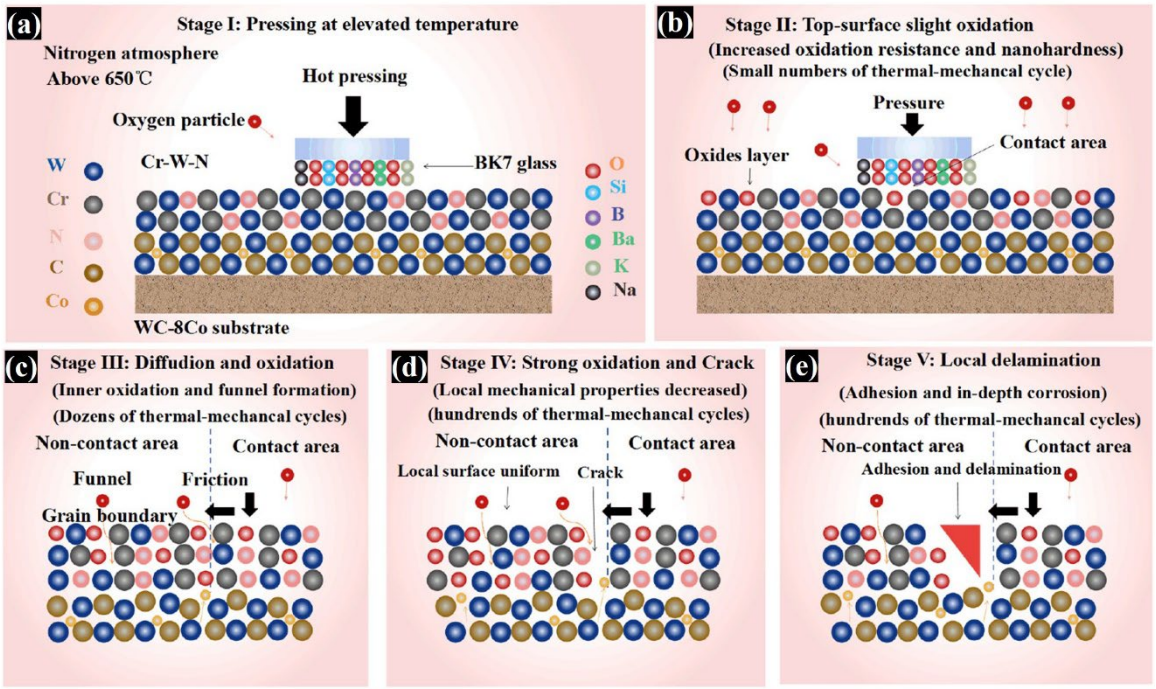

Figure 14. Illustration of the degradation mechanism of CrWN coatings in contact with BK7 optical glass [70]

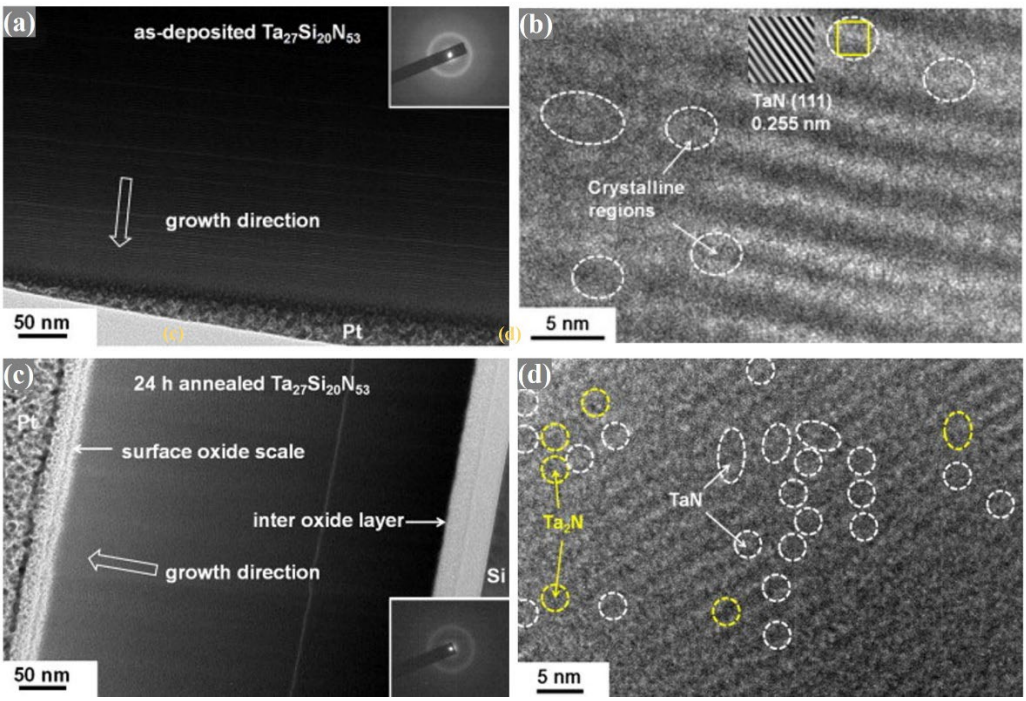

Figure 15. Cross-sectional TEM and HRTEM images of $Ta_{27}Si_{20}N_{53}$ coatings in the (a, b) as-deposited and (c, d) annealed states [56]

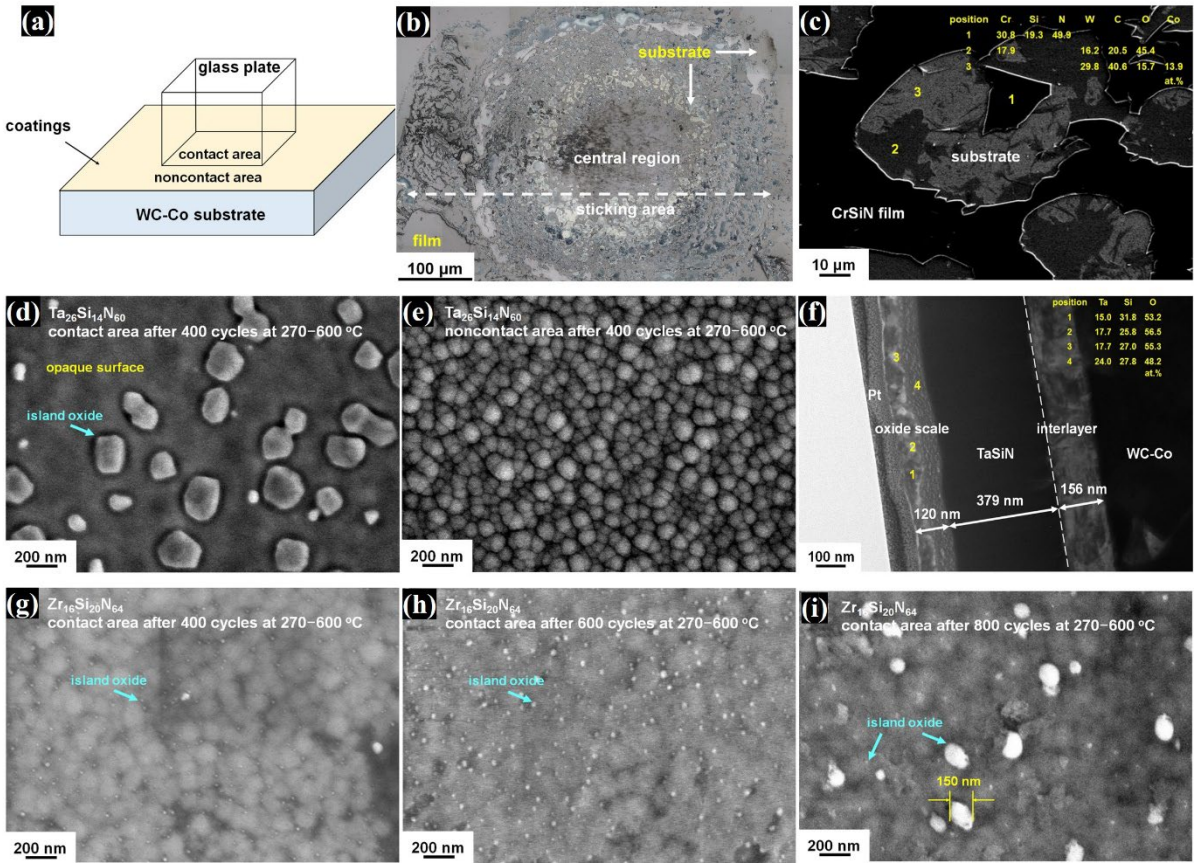

Figure 16. Study of SiN-based coatings: (a) schematic of glass/sample in heating test, SEM images of (b–c) $Cr_{28}Si_{17}N_{55}$ coatings, (d–f) $Ta_{26}Si_{14}N_{60}$ coatings, and (g–i) $Zr_{16}Si_{20}N_{64}$ coatings after heating [68]

3.4 Diamond-like carbon (DLC) coatings

DLC coatings encompass a wide range of carbon-based protective coatings. Owing to their high wear resistance and low coefficient of friction, they are generally used as protective layers against friction and various applications in which low friction is required [19]. The different properties of DLC coatings, such as chemical and mechanical properties, are determined by the sp^2/sp^3 content ratio as well as hydrogen content. The DLC coatings containing a high content (more than 40% [115] or 60%[101]) of sp^3-modification without any hydrogen are known as tetrahedral amorphous carbon (ta-C) coatings. These coatings have excellent properties, including high hardness, high density, low abrasion rates, and low chemical reactivity. Generally, PVD processes such as conventional sputtering can only induce less than 40% content of sp^3 because the carbon ions are unable to gain sufficient energy and are deposited on the substrate's surface with little momentum, resulting in inadequacy in the formation of sp^3 bonds. Consequently, most carbon particles accumulate in small grains,

resulting in graphite modification [116]. The deposition of (ta-C) DLC coatings with a high sp^3 content requires specialized deposition techniques such as filtered cathodic vacuum arc (FCVA) deposition, which are not commonly used in the industry. Bernhardt et al. [101] developed ta-C coatings with an sp^3 ratio of approximately 60% using magnetron sputtering ion plating (MSIP) on a WC substrate for glass molding applications and annealed in a vacuum environment with glass at different temperatures of 590 and 630 °C. Most of the coated surfaces corrugated after annealing because of residual stresses; only few of them kept a good smoothness of the surfaces. Zhang et al. [69] fabricated DLC coatings on WC substrates using FCVA and ion-assisted magnetron sputtering methods and reported that the occurrence of graphitization at temperatures above 450 °C dramatically affects the lifespan of coated molds in PGM. Although DLC coatings offer good self-lubrication with improved anti-wear properties, their poor thermal stability and the requirement of the dedicated coating facility restricts their applications in the glass molding industry [101, 117]. Additionally, although a few attempts have been made to employ DLC coatings for PGM applications, owing to the graphitization, it tends to oxidize at high temperatures and in an industrial production environment (e.g., with a constant N_2 flow), rendering it unsuitable for glasses with high T_g (e.g., $T_g \geq 550$ °C).

4. Tribological Performances

In addition to thermal/chemical stability and anti-stick performance, coatings must also have high toughness, high hardness, and low friction for PGM applications that involve the flow of glass on a coating surface. Among these, hardness is the most important for industrial coating applications involving contact and sliding [118]. Nanoindentation is employed to quantify it, in which a diamond-tipped indenter is forced into a coating surface. Subsequently, the elastic properties and hardness are determined based on the recorded force-indentation curve.

Nanoindentation is considered one of the fastest and simplest methods for obtaining information about the mechanical properties of thin films [119]. To avoid the influence of the substrate, a general rule of thumb to obtain precise measurements of hardness (H) and Young's modulus (E) of thin films is that the indentation depth must be less than one-tenth of the overall coating thickness [120]. During the process of loading and unloading in the nanoindentation method, the machine continually records the load (P) against indentation depth (h). After recording the P–h curve, the H can be determined as [121]

$$H = \frac{P_{max}}{A} \qquad (1)$$

where P_{max} is the maximum indentation load, and A represents the projected contact area between the specimen and indenter. The effective modulus (E_{ff}) can be calculated as [121]

$$E_{eff}=\frac{\sqrt{\pi}}{2}\frac{dp}{dh}\frac{1}{\sqrt{A}} \qquad (2)$$

where dp/dh is the slope of the (load–displacement) unloading curve at the maximum indentation depth. The elastic modulus of the indented material can then be calculated by substituting E_{eff} in the Eq (3).

$$\frac{1}{E_{eff}}=\frac{1-\upsilon^2}{E}+\frac{1-\upsilon_i^2}{E_i} \qquad (3)$$

where E_i and υ_i are the elastic modulus and Poisson's ratio of indenter, respectively, and E is the elastic modulus of the indented material.

Wei et al. [65] performed nanoindentation for monolayer and multilayer Re/Ir coatings and observed that the multilayer Re/Ir coating exhibited a higher Young's modulus and hardness than those of the monolayers (Re or Ir). The significant enhancement in the mechanical properties of the multilayered coating was determined to be primarily due to dislocation blockage by interfaces [122]. In addition, as the grain size is constrained by the layer thickness, the hindrance of dislocation increases with refinement in grain size, which results in higher hardness. Moreover, the multilayer structure can also contribute to the coating toughness [80] because the interfaces result in an enhancement in the resistance to crack propagation. Based on a series of studies on Re/Ir coatings, it appears that the multilayer design has an overwhelming advantage over monolayer coatings in terms of both tribological and chemical properties.

The nanoscratch test is also commonly used to determine the adhesive properties of coatings and thin films [123, 124], in which the lateral force is measured while moving an indenter tip that has been forced into the specimen [125]. Using a constant rate of increase in the normal force and a constant scratching speed, Klocke et al. [52] investigated the influence of the interlayer material and its thickness on the adhesion of the PtIr film. They observed that in the absence of an interlayer, a steep increase in the indentation depth was developed in the early stage of scratching and that the adhesion and hardness of the PtIr film were improved after depositing the Ni or Cr interlayer. The critical scratch load increased with the interlayer thickness, and the 50-nm Cr interlayer performed the best in resisting exfoliation. The probable reasons for the improvement in adhesion are the enhanced compatibility of the mechanical

properties between the coating and substrate and the establishment of stronger bonds at the interfacial area of the material.

In the load-control mode, a nanoindenter tip can repeatedly hit a coating surface with a prescribed maximum load. This is called a nanoimpact test [126], which may determine the toughness of the coatings. In the nanoimpact test, a solenoid is employed to drag the indenter from the surface and perform the re-acceleration from a short distance opposite to the film. The repetition of impacts at the same location is enabled by proper automation. The development of indentation depth against repetitive impacts is continually monitored. Thus, the progress of film deformation is captured. For the PtIr coatings, nanoimpact tests have been performed to study the effects of interlayers (Cr and Ni) with varying thicknesses [52]. The interlayer was observed to improve the resistance to repetitive impacts. In particular, with the employment of a Cr interlayer of 50 nm, the imprint depth remained almost unchanged up to nearly 1500 impacts. This result was ascribed to the plastic deformation of the film during several initial impacts and the work hardening effect to resist further impacts. For all other examined scenarios, a progressive film fracture occurred as the number of impacts increased, resulting in a continuous increase in the imprint depth. Consequently, it was concluded that the Cr interlayer with a thickness of 50 nm provided a significant toughening effect on the entire coating structure to withstand repetitive impact loading. Conversely, the coatings without adhesive interlayer coatings failed rapidly during the impact tests.

Huang et al. [67] determined the mechanical properties of CrWN coatings through nanoindentation. They observed that co-sputtered coatings with increased W content after annealing at 650 °C resulted in higher hardness, and coatings with a high H/E (i.e., hardness over Young's modulus) ratio demonstrated good fracture toughness. In another study, Huang et al. [127] compared the mechanical performance of CrWN coatings heated at 650 °C in vacuum, nitrogen, and air environments. The evaluation using nanoindentation demonstrated that the vacuum-annealed coatings exhibited a noticeable age-hardening effect, and therefore, the significant improvement in mechanical properties was ascribed to spinodal decomposition. In contrast, the CrWN coatings annealed in nitrogen and air environments suffered from substantial mechanical degradation caused by oxidative damage. Chang et al. [128] evaluated the hardness of Hf-Si-N coatings using nanoindentation and observed that the hardness of the coatings after annealing (at 600 °C) initially increased and then decreased with continuous annealing (100 h), owing to the formation of an oxide scale on the surface. Guo et al. [71] examined the mechanical performance of CrWN coatings before and after annealing at 650 °C under vacuum and concluded that both the nanohardness and Young's modulus increased after

annealing owing to the occurrence of an age-hardening mechanism. Although these studies have demonstrated the tribological performances of the various PGM coatings, it is unclear how the room-temperature performances correlate with high-temperature ones or with the lifetime of coatings in PGM cycles. The measurements of high-temperature tribological performances and the development of quantitative models revealing the influence of various degradation mechanisms are therefore suggested for the future studies.

5. Summary and outlook

This paper summarizes the major coating techniques and reviews the coating performance of PGM applications. Glass molding tools must have high-temperature strength and significant resistance to wear and oxidation, which can be achieved using a suitable selection of coating material and process. Previous studies have reported that PtIr coatings with various interlayers are the most widely employed molding tools to achieve anti-sticking properties and thermal stability in PGM. However, these coatings may suffer from oxidation and glass-sticking problems, where a higher temperature (> 700 °C) is required. In addition, Ir is costly. Therefore, to overcome these problems, a new coating system is required. In the noble metal group, Ru has a superior oxidation resistance and better mechanical properties, and it can be a potential candidate for PGM at high temperatures. In addition, the cost of Ru is significantly lower than that of Ir. Ceramic coatings may still have a role in future coating developments for PGMs because of their lower cost compared with noble metals. Conventional nitrides, such as CrWN, CrN, and TiAlN, have been attempted. However, their performance in PGM is barely satisfactory because of the reaction and adhesion with glass. Instead, silicon-nitride-based coatings such as ZrSiN may be used as proscriptive coatings for glass molding owing to their enhanced oxidation resistance due to the introduction of silicon.

Note that the study of coatings for PGM is still in its infancy, as existing experimental results do not provide a sufficient dataset to develop theoretical or computational models to predict coating failure and optimize coating design. While the mechanism of coating failures, through either the diffusion of active elements in noble metal systems or by the oxidation of metallic elements in ceramic coatings, have been revealed in a few recent publications, it is expected that more in-depth studies must be conducted to achieve quantitative models of coatings that relate mold life with various process and coating parameters (e.g., temperature, coating materials, layer thickness, etc.). These models will aid in designing cost-effective coatings for engineering applications.

Acknowledgment

We gratefully acknowledge the financial support provided by the Hong Kong GRF (Grant No. 15213619).

References

1. Zhang, Y.; Yan, G.; Li, Z.; Fang, F. Quality improvement of collimating lens produced by precision glass molding according to performance evaluation. *Optics express,* **2019**, 27, 5033-5047.
2. He, P.; Li, L.; Wang, F.; Dambon, O.; Klocke, F.; Flores, K. M.; Allen, Y. Y. Bulk metallic glass mold for high volume fabrication of micro optics. *Microsystem Technologies,* **2016**, 22, 617-623.
3. Zhou, T.; Liu, X.; Liang, Z.; Liu, Y.; Xie, J.; Wang, X. Recent advancements in optical microstructure fabrication through glass molding process. *Frontiers of Mechanical Engineering,* **2017**, 12, 46-65.
4. Liu, W.; Zhang, L. Thermoforming mechanism of precision glass moulding. *Applied optics,* **2015**, 54, 6841-6849.
5. Brinksmeier, E.; Mutlugünes, Y.; Klocke, F.; Aurich, J.; Shore, P.; Ohmori, H. Ultra-precision grinding. *CIRP annals,* **2010**, 59, 652-671.
6. Yi, A.; Jain, A. Experimental and numerical analysis compression molding of aspherical glass lenses-A combined. *Journal of the American Ceramic Society,* **2005**, 88, 579-586.
7. Deng, L.; Zhao, R. A vibration analysis method based on hybrid techniques and its application to rotating machinery. *Measurement,* **2013**, 46, 3671-3682.
8. Ma, K. J.; Chien, H.; Chuan, W.; Chao, C. L.; Hwang, K. *Design of protective coatings for glass lens molding*. in *Key Engineering Materials*. 2008. Trans Tech Publ.
9. Kang, C.-Y.; Chen, Y.-I.; Lin, C.-H.; Duh, J.-G. Mechanical properties of Mo–Ru thin films with Ni interlayer of different thickness. *Applied surface science,* **2007**, 253, 6191-6195.
10. Vaz, F.; Rebouta, L. *Superhard nanocomposite ti-si-n coatings*. in *Materials science forum*. 2002. Trans Tech Publ.
11. Anders, S.; Anders, A.; Kortright, J.; Yu, K. M.; Brown, I.; Ivanov, I. Vacuum arc deposition of multilayer X-ray mirrors. *Surface and Coatings Technology,* **1993**, 61, 257-261.
12. Bemporad, E.; Sebastiani, M.; Pecchio, C.; De Rossi, S. High thickness Ti/TiN multilayer thin coatings for wear resistant applications. *Surface and Coatings Technology,* **2006**, 201, 2155-2165.
13. Zhang, L.; Liu, W. Precision glass molding: Toward an optimal fabrication of optical lenses. *Frontiers of Mechanical Engineering,* **2017**, 12, 3-17.
14. Chao, C. L.; Huo, C. B.; Chou, W.-C.; Lin, Y. R.; Ma, K. J.; Chien, H. H. Study on the design of precious metal based protective films for glass moulding process. *Surface and Coatings Technology,* **2013**, 231, 567-572.
15. Zhang, L.; Liu, G.; Zhao, X.; Dambon, O.; Klocke, F.; Yi, A. *Precision molding of optics: a review of its development and applications*. in *Polymer Optics and Molded Glass Optics: Design, Fabrication, and Materials 2016*. 2016. International Society for Optics and Photonics.
16. Upadhyaya, G. S., *Cemented tungsten carbides: production, properties and testing*. 1998: William Andrew.
17. Bobzin, K.; Bagcivan, N. Correlation between chemical glass components and the glass sticking on sputtered PtIr physical vapour deposition coatings for precision blank moulding. *Materials sciences and applications,* **2014**, 2014.
18. Mayrhofer, P. H.; Tischler, G.; Mitterer, C. Microstructure and mechanical/thermal properties of Cr–N coatings deposited by reactive unbalanced magnetron sputtering. *Surface and Coatings Technology,* **2001**, 142, 78-84.
19. Brand, J.; Gadow, R.; Killinger, A. Application of diamond-like carbon coatings on steel tools in the production of precision glass components. *Surface and Coatings Technology,* **2004**, 180, 213-217.

20. Toku, H.; Pessoa, R.; Maciel, H.; Massi, M.; Mengui, U. Influence of process parameters on the growth of pure-phase anatase and rutile TiO2 thin films deposited by low temperature reactive magnetron sputtering. *Brazilian Journal of Physics,* **2010**, 40, 340-343.
21. Alami, J., *Plasma Characterization & Thin Film Growth and Analysis in Highly Ionized Magnetron Sputtering*. 2005, Institutionen för fysik, kemi och biologi.
22. Hashmi, S., *Comprehensive materials processing*. 2014: Newnes.
23. Martin, P., *Introduction to surface engineering and functionally engineered materials*. Vol. 74. 2011: John Wiley & Sons.
24. Martin, P. M., *Handbook of deposition technologies for films and coatings: science, applications and technology*. 2009: William Andrew.
25. Aliofkhazraei, M.; Ali, N. PVD Technology in fabrication of micro-and nanostructured coatings. **2014**.
26. Tung, S.; Cheng, Y. *Tribological characteristics and microstructures of PVD thin film coatings on steel substrates*. in *Proceedings of the International Wear Conference, San Francisco, California*. 1993.
27. Okumiya, M.; Griepentrog, M. Mechanical properties and tribological behavior of TiN–CrAlN and CrN–CrAlN multilayer coatings. *Surface and Coatings Technology,* **1999**, 112, 123-128.
28. Schiller, S.; Goedicke, K.; Reschke, J.; Kirchhoff, V.; Schneider, S.; Milde, F. Pulsed magnetron sputter technology. *Surf. Coat. Technol,* **1993**, 61, 331-337.
29. Bewilogua, K.; Bräuer, G.; Dietz, A.; Gäbler, J.; Goch, G.; Karpuschewski, B.; Szyszka, B. Surface technology for automotive engineering. *CIRP annals,* **2009**, 58, 608-627.
30. Mattox, D. M.; Mattox, V. H. *years of vacuum coating technology and the growth of the Society of Vacuum Coaters*. in *Society of Vacuum Coaters*. 2007.
31. Metzner, C.; Scheffel, B. Special aspects concerning the electron beam deposition of multi-component alloys. *Surface and Coatings Technology,* **2001**, 146, 491-497.
32. Lokhande, A.; Chalapathy, R.; He, M.; Jo, E.; Gang, M.; Pawar, S.; Lokhande, C.; Kim, J. H. Development of Cu2SnS3 (CTS) thin film solar cells by physical techniques: A status review. *Solar Energy Materials and Solar Cells,* **2016**, 153, 84-107.
33. Jilani, A.; Abdel-Wahab, M. S.; Hammad, A. H. Advance deposition techniques for thin film and coating. *Modern Technologies for Creating the Thin-film Systems and Coatings,* **2017**, 2, 137-149.
34. Seong, J.-W.; Yoon, K. Effect of oxygen content on barrier properties of silicon oxide thin film deposited by dual ion-beam sputtering. *Journal of non-crystalline solids,* **2006**, 352, 84-91.
35. Wang, G.; Zreiqat, H. Functional coatings or films for hard-tissue applications. *Materials,* **2010**, 3, 3994-4050.
36. Abegunde, O. O.; Akinlabi, E. T.; Oladijo, O. P.; Akinlabi, S.; Ude, A. U. Overview of thin film deposition techniques. *AIMS Materials Science,* **2019**, 6, 174.
37. Kommu, S.; Wilson, G. M.; Khomami, B. A theoretical/experimental study of silicon epitaxy in horizontal single‐wafer chemical vapor deposition reactors. *Journal of The Electrochemical Society,* **2000**, 147, 1538.
38. Pedersen, H.; Elliott, S. D. Studying chemical vapor deposition processes with theoretical chemistry. *Theoretical Chemistry Accounts,* **2014**, 133, 1476.
39. Seshan, K., *Handbook of thin film deposition processes and techniques*. 2001: William Andrew.
40. Wu, F.-b.; Chen, W.-y.; Duh, J.-g.; Tsai, Y.-y.; Chen, Y.-i. Ir-based multi-component coating on tungsten carbide by RF magnetron sputtering process. *Surface and Coatings Technology,* **2003**, 163, 227-232.
41. Lin, C.-H.; Duh, J.-G.; Yau, B.-S. Processing of chromium tungsten nitride hard coatings for glass molding. *Surface and Coatings Technology,* **2006**, 201, 1316-1322.
42. Chen, Y.-I.; Liu, K.-T.; Wu, F.-B.; Duh, J.-G. Mo–Ru coatings on tungsten carbide by direct current magnetron sputtering. *Thin solid films,* **2006**, 515, 2207-2212.

43. Wen, S.; Zong, R.; Zeng, F.; Gu, Y.; Gao, Y.; Pan, F. Thermal stability of microstructure and mechanical properties of Ni/Ru multilayers. *Surface and Coatings Technology,* **2008**, 202, 2040-2046.
44. Chen, Y.-I.; Chang, L.-C.; Lee, J.-W.; Lin, C.-H. Annealing and oxidation study of Mo–Ru hard coatings on tungsten carbide. *Thin Solid Films,* **2009**, 518, 194-200.
45. Chien, H. H.; Ma, K. J.; Kuo, C. H.; Huo, C. B.; Chao, C. L.; Chen, Y. T. *The effect of TaN interlayer on the performance of Pt-Ir protective coatings in glass molding process*. in *Defect and Diffusion Forum*. 2010. Trans Tech Publ.
46. Bobzin, K.; Klocke, F.; Bagcivan, N.; Ewering, M.; Georgiadis, K.; Münstermann, T. *Impact behaviour of PtIr-based coatings with different interlayers for glass lens moulding*. in *Key Engineering Materials*. 2010. Trans Tech Publ.
47. Sakurai, J.; Hata, S.; Yamuchi, R.; Abe, M.; Shimokohbe, A. Searching for Pt–Zr–Ni thin film amorphous alloys for optical glass lenses molding materials. *Precision Engineering,* **2010**, 34, 431-439.
48. Fischbach, K. D.; Georgiadis, K.; Wang, F.; Dambon, O.; Klocke, F.; Chen, Y.; Allen, Y. Y. Investigation of the effects of process parameters on the glass-to-mold sticking force during precision glass molding. *Surface and Coatings Technology,* **2010**, 205, 312-319.
49. Masuda, J.; Yan, J.; Zhou, T.; Kuriyagawa, T.; Fukase, Y. Thermally induced atomic diffusion at the interface between release agent coating and mould substrate in a glass moulding press. *Journal of Physics D: Applied Physics,* **2011**, 44, 215302.
50. Chen, Y.-I.; Lin, B.-L.; Kuo, Y.-C.; Huang, J.-C.; Chang, L.-C.; Lin, Y.-T. Preparation and annealing study of TaNx coatings on WC-Co substrates. *Applied surface science,* **2011**, 257, 6741-6749.
51. Tseng, S.-F.; Lee, C.-T.; Huang, K.-C.; Chiang, D.; Huang, C.-Y.; Chou, C.-P. Mechanical properties of Pt-Ir and Ni-Ir binary alloys for glass-molding dies coating. *Journal of nanoscience and nanotechnology,* **2011**, 11, 8682-8688.
52. Klocke, F.; Bouzakis, K.-D.; Georgiadis, K.; Gerardis, S.; Skordaris, G.; Pappa, M. Adhesive interlayers' effect on the entire structure strength of glass molding tools' Pt–Ir coatings by nano-tests determined. *Surface and Coatings Technology,* **2011**, 206, 1867-1872.
53. Bobzin, K.; Bagcivan, N.; Ewering, M.; Brugnara, R.; Münstermann, T. Influence of interlayer thickness of a thin noble metal MSIP-PVD coating on compound and system properties for glass lens moulding. *Production Engineering,* **2012**, 6, 311-318.
54. Lin, T.-N.; Han, S.; Weng, K.-W.; Lee, C.-T. Investigation on the structural and mechanical properties of anti-sticking sputtered tungsten chromium nitride films. *Thin Solid Films,* **2013**, 529, 333-337.
55. Liu, S.-C.; Chen, Y.-I.; Tsai, H.-Y.; Lin, K.-C.; Chen, Y.-H. Thermal stability of Ir–Re coatings annealed in oxygen-containing atmospheres. *Surface and Coatings Technology,* **2013**, 237, 105-111.
56. Chen, Y.-I.; Lin, K.-Y.; Wang, H.-H.; Cheng, Y.-R. Characterization of Ta–Si–N coatings prepared using direct current magnetron co-sputtering. *Applied surface science,* **2014**, 305, 805-816.
57. Chen, Y.-I.; Lin, K.-Y.; Wang, H.-H.; Lin, K.-C. Thermal stability of TaN, CrTaN, TaSiN, and CrTaSiN hard coatings in oxygen-containing atmospheres. *Surface and Coatings Technology,* **2014**, 259, 159-166.
58. Chen, Y.-I.; Wang, H.-H. Oxidation resistance and mechanical properties of Cr–Ta–Si–N coatings in glass molding processes. *Surface and Coatings Technology,* **2014**, 260, 118-125.
59. Zhu, X.-y.; Wei, J.-j.; Chen, L.-x.; Liu, J.-l.; Hei, L.-f.; Li, C.-m.; Zhang, Y. Anti-sticking Re-Ir coating for glass molding process. *Thin Solid Films,* **2015**, 584, 305-309.
60. Chen, Y.-I.; Cheng, Y.-R.; Chang, L.-C.; Lee, J.-W. Chemical inertness of Cr–W–N coatings in glass molding. *Thin Solid Films,* **2015**, 593, 102-109.

61. Klocke, F.; Dambon, O.; Rohwerder, M.; Bernhardt, F.; Friedrichs, M.; Merzlikin, S. V. Model of coating wear degradation in precision glass molding. *The International Journal of Advanced Manufacturing Technology,* **2016**, 87, 43-49.
62. Peng, Z.; Rohwerder, M.; Choi, P.-P.; Gault, B.; Meiners, T.; Friedrichs, M.; Kreilkamp, H.; Klocke, F.; Raabe, D. Atomic diffusion induced degradation in bimetallic layer coated cemented tungsten carbide. *Corrosion Science,* **2017**, 120, 1-13.
63. Chang, L.-C.; Zheng, Y.-Z.; Chen, Y.-I.; Chang, S.-C.; Liu, B.-W. Bonding characteristics and chemical inertness of Zr–Si–N coatings with a high Si content in glass molding. *Coatings,* **2018**, 8, 181.
64. Lee, S.-H.; Ko, I.-H.; Kim, T.-Y. Surface failure analysis of AlCrN coating on WC substrate subjected to high-temperature oxidation in glass-molding machine. *Applied Surface Science,* **2018**, 452, 210-216.
65. Wei, J.; Zhu, X.; Chen, L.; Liu, J.; Li, C. High quality anti-sticking coating based on multilayer structure. *Surface and Coatings Technology,* **2019**, 362, 72-77.
66. Friedrichs, M.; Peng, Z.; Grunwald, T.; Rohwerder, M.; Gault, B.; Bergs, T. PtIr protective coating system for precision glass molding tools: Design, evaluation and mechanism of degradation. *Surface and Coatings Technology,* **2020**, 385, 125378.
67. Huang, X.; Xie, Z.; Li, K.; Chen, Q.; Gong, F.; Chen, Y.; Feng, B.; Hu, S.; Chen, Y.; Han, B. Microstructure, wear and oxidation resistance of CrWN glass molding coatings synthesized by plasma enhanced magnetron sputtering. *Vacuum,* **2020**, 174, 109206.
68. Chen, Y.-I.; Ke, Y.-E.; Sung, M.-C.; Chang, L.-C. Rapid thermal annealing of Cr–Si–N, Ta–Si–N, and Zr–Si–N coatings in glass molding atmospheres. *Surface and Coatings Technology,* **2020**, 389, 125662.
69. Zhang, Y.; Yan, G.; You, K.; Fang, F. Study on α-Al2O3 anti-adhesion coating for molds in precision glass molding. *Surface and Coatings Technology,* **2020**, 391, 125720.
70. Li, K.; Xu, G.; Huang, X.; Chen, Q.; Xie, Z.; Gong, F. Surface evolution analysis of CrxWyNz coatings on WC mold in glass molding process. *Surface and Coatings Technology,* **2020**, 393, 125839.
71. Guo, F.; Huang, X.; Xie, Z.; Li, K.; Gong, F.; Chen, Y.; Chen, Q. Understanding the age-hardening mechanism of CrWN coating. *Thin Solid Films,* **2020**, 711, 138298.
72. Klocke, F.; Bergs, T.; Georgiadis, K.; Sarikaya, H.; Wang, F. *Coating systems for precision glass molding tools*. in *Proc. 7th Int. Conf. Coatings Manuf. Eng*. 2008.
73. Klocke, F.; Dambon, O.; Georgiadis, K. *Comparison of nitride and noble metal coatings for precision glass molding tools*. in *Key Engineering Materials*. 2010. Trans Tech Publ.
74. Zhong, D.; Mateeva, E.; Dahan, I.; Moore, J.; Mustoe, G.; Ohno, T.; Disam, J.; Thiel, S. Wettability of NiAl, Ni Al N, Ti B C, and Ti B–C N films by glass at high temperatures. *Surface and Coatings Technology,* **2000**, 133, 8-14.
75. Lyeo, H.-K.; Cahill, D. G. Thermal conductance of interfaces between highly dissimilar materials. *Physical Review B,* **2006**, 73, 144301.
76. Gundrum, B. C.; Cahill, D. G.; Averback, R. S. Thermal conductance of metal-metal interfaces. *Physical Review B,* **2005**, 72, 245426.
77. Bull, S.; Jones; AM Multilayer coatings for improved performance. *Surface and Coatings Technology,* **1996**, 78, 173-184.
78. Khadem, M.; Penkov, O. V.; Yang, H.-K.; Kim, D.-E. Tribology of multilayer coatings for wear reduction: A review. *Friction,* **2017**, 5, 248-262.
79. Yang, Q.; Zhao, L. Thermal stability of polycrystalline TiN/CrN superlattice coatings. *Journal of Vacuum Science & Technology A: Vacuum, Surfaces, and Films,* **2003**, 21, 558-562.
80. Chu, X.; Barnett, S. A. Model of superlattice yield stress and hardness enhancements. *Journal of Applied Physics,* **1995**, 77, 4403-4411.
81. Brown, A.; Ashby, M. Correlations for diffusion constants. *Acta Metallurgica,* **1980**, 28, 1085-1101.

82. Mehrer, H., *Diffusion in solids: fundamentals, methods, materials, diffusion-controlled processes*. Vol. 155. 2007: Springer Science & Business Media.
83. Harrison, L. Influence of dislocations on diffusion kinetics in solids with particular reference to the alkali halides. *Transactions of the Faraday Society,* **1961**, 57, 1191-1199.
84. Poate, J.; Turner, P.; DeBonte, W.; Yahalom, J. Thin-film interdiffusion. I. Au-Pd, Pd-Au, Ti-Pd, Ti-Au, Ti-Pd-Au, and Ti-Au-Pd. *Journal of Applied Physics,* **1975**, 46, 4275-4283.
85. Tompkins, H.; Pinnel, M. Low-temperature diffusion of copper through gold. *Journal of Applied Physics,* **1976**, 47, 3804-3812.
86. Chang, C. A. Effect of CO on the low temperature diffusion of Cr and Si through thin gold films. *Journal of The Electrochemical Society,* **1980**, 127, 1331.
87. Lee, J.; Jeong, H.; Yoon, C. S.; Kim, C. K.; Park, B. G.; Lee, T. D. Interdiffusion in antiferromagnetic/ferromagnetic exchange coupled NiFe/IrMn/CoFe multilayer. *Journal of applied physics,* **2002**, 91, 1431-1435.
88. Rairden, J.; Neugebauer, C.; Sigsbee, R. Interdiffusion in thin conductor films—chromium/gold, nickel/gold and chromium silicide/gold. *Metallurgical Transactions,* **1971**, 2, 719-722.
89. Hiraki, A.; Lugujjo, E.; Mayer, J. W. Formation of silicon oxide over gold layers on silicon substrates. *Journal of Applied Physics,* **1972**, 43, 3643-3649.
90. Tompkins, H.; Pinnel, M. Relative rates of nickel diffusion and copper diffusion through gold. *Journal of Applied Physics,* **1977**, 48, 3144-3146.
91. Gösele, U.; Tu, K.-N. Growth kinetics of planar binary diffusion couples:''Thin-film case'' versus''bulk cases''. *Journal of Applied Physics,* **1982**, 53, 3252-3260.
92. Canali, C.; Catellani, F.; Ottaviani, G.; Prudenziati, M. On the formation of Ni and Pt silicide first phase: the dominant role of reaction kinetics. *Applied Physics Letters,* **1978**, 33, 187-190.
93. Ottaviani, G. Review of binary alloy formation by thin film interactions. *Journal of vacuum science and technology,* **1979**, 16, 1112-1119.
94. Ottaviani, G.; Costato, M. Compound formation in metal—semiconductor interactions. *Journal of Crystal Growth,* **1978**, 45, 365-375.
95. Colgan, E.; Tsaur, B.; Mayer, J. Phase formation in Cr-Si thin-film interactions. *Applied Physics Letters,* **1980**, 37, 938-940.
96. Tu, K.-N. Interdiffusion in thin films. *Annual Review of Materials Science,* **1985**, 15, 147-176.
97. Poate, J. M.; Tu, K.-n.; Mayer, J. W., *Thin films: interdiffusion and reactions*. 1978: John Wiley & Sons.
98. Zeng, K.; Stierman, R.; Chiu, T.-C.; Edwards, D.; Ano, K.; Tu, K.-N. Kirkendall void formation in eutectic SnPb solder joints on bare Cu and its effect on joint reliability. *Journal of applied physics,* **2005**, 97, 024508.
99. Paul, A.; Laurila, T.; Vuorinen, V.; Divinski, S. V., *Thermodynamics, diffusion and the Kirkendall effect in solids*. 2014: Springer.
100. Springer, H.; Kostka, A.; Dos Santos, J. F.; Raabe, D. Influence of intermetallic phases and Kirkendall-porosity on the mechanical properties of joints between steel and aluminium alloys. *Materials Science and Engineering: A,* **2011**, 528, 4630-4642.
101. Bernhardt, F.; Georgiadis, K.; Dolle, L.; Dambon, O.; Klocke, F. Development of a ta-C diamond-like carbon (DLC) coating by magnetron sputtering for use in precision glass molding. *Materialwissenschaft und Werkstofftechnik,* **2013**, 44, 661-666.
102. He, P.; Li, L.; Yu, J.; Huang, W.; Yen, Y.-C.; Lee, L. J.; Allen, Y. Y. Graphene-coated Si mold for precision glass optics molding. *Optics letters,* **2013**, 38, 2625-2628.
103. Liu, S.-C.; Chen, Y.-I.; Shyu, J.-J.; Tsai, H.-Y.; Lin, K.-Y.; Chen, Y.-H.; Lin, K.-C. The chemical inertness of Ir–Re and Ta–Ru coatings in molding B2O3–ZnO–La2O3-based glass. *Surface and Coatings Technology,* **2014**, 259, 352-357.

104. Chen, Y.-I.; Tsai, B.-N. Internal oxidation mechanism for Ta–Ru and Mo–Ru coatings. *Thin solid films,* **2011**, 519, 4974-4980.
105. Bajt, S.; Nelson, E. J.; Wall, M. A.; Alameda, J.; Nguyen, N.; Baker, S.; Robinson, J. C.; Taylor, J. S.; Clift, M.; Aquila, A. *Oxidation resistance of Ru-capped EUV multilayers*. in *Emerging Lithographic Technologies IX*. 2005. International Society for Optics and Photonics.
106. Lee, H.; Coutu, R. A.; Mall, S.; Leedy, K. D. Characterization of metal and metal alloy films as contact materials in MEMS switches. *Journal of Micromechanics and Microengineering,* **2006**, 16, 557.
107. Li, C.; Dai, R.; Qi, R.; Wu, X.; Ma, J. Electrodeposition of Pt–Ru alloy electrocatalysts for direct methanol fuel cell. *Int. J. Electrochem. Sci,* **2017**, 12, 2485-2494.
108. Han, J. H.; Lee, S. W.; Choi, G.-J.; Lee, S. Y.; Hwang, C. S.; Dussarrat, C.; Gatineau, J. Chemical vapor deposition of Ru thin films with an enhanced morphology, thermal stability, and electrical properties using a RuO4 precursor. *Chemistry of Materials,* **2009**, 21, 207-209.
109. Chen, Y.-I.; Tsai, B.-N. Annealing and oxidation study of Ta–Ru hard coatings. *Surface and Coatings Technology,* **2010**, 205, 1362-1367.
110. Khanna, A. S., *Introduction to high temperature oxidation and corrosion*. 2002: ASM international.
111. Douglass, D. A critique of internal oxidation in alloys during the post-Wagner era. *Oxidation of Metals,* **1995**, 44, 81-111.
112. Chen, Y.-I.; Kuo, Y.-C.; Chen, S.-M. Oxidation study of Cr–Ru hard coatings. *Thin solid films,* **2012**, 520, 2066-2072.
113. Wuhrer, R.; Yeung, W. Grain refinement with increasing magnetron discharge power in sputter deposition of nanostructured titanium aluminium nitride coatings. *Scripta Materialia,* **2004**, 50, 813-818.
114. Hones, P.; Consiglio, R.; Randall, N.; Levy, F. Mechanical properties of hard chromium tungsten nitride coatings. *Surface and Coatings Technology,* **2000**, 125, 179-184.
115. Kalish, R.; Lifshitz, Y.; Nugent, K.; Prawer, S. Thermal stability and relaxation in diamond-like-carbon. A Raman study of films with different sp 3 fractions (ta-C to a-C). *Applied physics letters,* **1999**, 74, 2936-2938.
116. Schwan, J.; Ulrich, S.; Roth, H.; Ehrhardt, H.; Silva, S.; Robertson, J.; Samlenski, R.; Brenn, R. Tetrahedral amorphous carbon films prepared by magnetron sputtering and dc ion plating. *Journal of applied physics,* **1996**, 79, 1416-1422.
117. Xie, Z.; Wang, L.; Wang, X.; Huang, L.; Lu, Y.; Yan, J. Influence of high temperature annealing on the structure, hardness and tribological properties of diamond-like carbon and TiAlSiCN nanocomposite coatings. *Applied surface science,* **2011**, 258, 1206-1211.
118. Zhang, S.; Sun, D.; Fu, Y.; Du, H. Recent advances of superhard nanocomposite coatings: a review. *Surface and Coatings Technology,* **2003**, 167, 113-119.
119. Bouzakis, K.-D.; Hadjiyiannis, S.; Skordaris, G.; Anastopoulos, J.; Mirisidis, I.; Michailidis, N.; Efstathiou, K.; Knotek, O.; Erkens, G.; Cremer, R. The influence of the coating thickness on its strength properties and on the milling performance of PVD coated inserts. *Surface and Coatings Technology,* **2003**, 174, 393-401.
120. Nix, W. D. Mechanical properties of thin films. *Metallurgical transactions A,* **1989**, 20, 2217.
121. Oliver, W. C.; Pharr, G. M. Measurement of hardness and elastic modulus by instrumented indentation: Advances in understanding and refinements to methodology. *Journal of materials research,* **2004**, 19, 3-20.
122. Yu-Zhang, K.; Embury, J.; Han, K.; Misra, A. Transmission electron microscopy investigation of the atomic structure of interfaces in nanoscale Cu–Nb multilayers. *Philosophical Magazine,* **2008**, 88, 2559-2567.
123. Tomastik, J.; Ctvrtlik, R. *Nanoscratch test—A tool for evaluation of cohesive and adhesive properties of thin films and coatings*. in *EPJ web of conferences*. 2013. EDP Sciences.

124. Beake, B.; Harris, A.; Liskiewicz, T. Review of recent progress in nanoscratch testing. *Tribology-Materials, Surfaces & Interfaces,* **2013**, 7, 87-96.
125. Kartsonakis, I.; Balaskas, A.; Koumoulos, E.; Charitidis, C.; Kordas, G. Incorporation of ceramic nanocontainers into epoxy coatings for the corrosion protection of hot dip galvanized steel. *Corrosion science,* **2012**, 57, 30-41.
126. Frutos, E.; González-Carrasco, J. L.; Polcar, T. Repetitive nano-impact tests as a new tool to measure fracture toughness in brittle materials. *Journal of the European Ceramic Society,* **2016**, 36, 3235-3243.
127. Huang, X.; Xie, Z.; Li, K.; Chen, Q.; Gong, F.; Chen, Y.; Feng, B.; Chen, Y.; Wan, Y. Effect of annealing environment on the microstructure and mechanical property of CrWN glass molding coating. *Surface and Coatings Technology,* **2020**, 383, 125281.
128. Chang, L.-C.; Liu, B.-W.; Chen, Y.-I. Mechanical properties and oxidation behavior of multilayered Hf–Si–N coatings. *Coatings,* **2018**, 8, 354.